Regional Water Vapor Distribution and its Clear Sky Longwave Radiative Effects

by
Henry J. Ganse

Department of Atmospheric Science
Colorado State University
Fort Collins, Colorado

Colorado State University

Department of Atmospheric Science

Paper No. 569

REGIONAL WATER VAPOR DISTRIBUTION AND ITS CLEAR SKY LONGWAVE RADIATIVE EFFECTS

by

Henry J. Ganse

Research supported by NASA Grant NAGW-2700

Principal Investigator: Thomas H. Vonder Haar

Fall, 1994

Atmospheric Science Paper No. 569

This paper was also submitted in partial fulfillment of the requirements for the degree of Masters of Science.

ABSTRACT

REGIONAL WATER VAPOR DISTRIBUTION

AND ITS CLEAR SKY LONGWAVE RADIATIVE EFFECTS

Water vapor is the principal greenhouse gas and regulates the longwave radiation balance of the atmosphere. One physical measure of water vapor is the precipitable water, which is defined as the depth to which water would stand if it were completely condensed out of an atmospheric column. The research conducted in this thesis was divided into three studies to examine the distribution and variability of precipitable water as well as investigate the radiative effects of water vapor on the longwave radiation balance of the clear sky atmosphere.

The first study utilized a global, high resolution precipitable water dataset produced from blended radiosonde and satellite observations. The goal was to investigate the monthly distribution and variability of precipitable water on a regional scale covering the United States. Results indicated that precipitable water is a highly variably quantity in both time and space. Its variations were related to its latitudinal position on the globe, the nature of the land surface below, the general circulation, and the season of the year.

The availability of the data allowed for a study of the possible link between the precipitable water and the extensive drought conditions over the midwestern United States during the summer of 1988. Difference maps constructed for 1989 minus 1988 monthly averaged precipitable water showed great interannual variability. Evidence that the Gulf of Mexico was not able to provide moisture to the Midwest was found during May and June of 1988. Yet, no overwhelming deficit of precipitable water was found to exist during the entire spring and summer of 1988.

As the primary greenhouse gas, water vapor has a profound effect on the longwave radiation balance of the atmosphere. Water vapor selectively absorbs infrared radiation emitted from the surface and atmosphere and emits it to space at a lower temperature. Thus, the surface and atmospheric temperature of the planet are much warmer than if water vapor were not present.

The effects of water vapor on the clear sky outgoing longwave radiation (OLR) over land were examined. Satellite measurements of clear sky OLR were not produced from the ERBE averaging system on a daily basis due to insufficient sampling of the diurnal cycle. Surface temperatures collected by the International Satellite Cloud Climatology Project (ISCCP) were converted to surface fluxes and used to interpolate missing hourly data in the ERBE database. From these existing and interpolated hourly data, daily and monthly averages of clear sky OLR over land were calculated. The monthly averages computed from interpolated daily values showed good agreement with monthly mean clear sky OLR produced by the ERBE averaging system.

The relationships among precipitable water, surface and atmospheric temperatures, and clear sky OLR were explored with the aid of the LOWTRAN7 radiative transfer model. Three simulations using 1) observed values of precipitable water and temperature, 2) observed temperatures with precipitable water amounts held constant, and 3) observed precipitable water amounts with temperature held constant were run to calculate clear sky OLR over land.

The results indicated that temperature exerted the strongest influence over clear sky OLR. In both simulations using observed temperatures, the clear sky OLR showed a positive correlation with surface and atmospheric temperatures. The water vapor/clear sky OLR signal was less easily deciphered from the observations. Only when the temperature

was held constant, did the true relationship between precipitable water and clear sky OLR become evident. In the absence of temperature variations, an increase in precipitable water, especially at middle and upper tropospheric levels, led to a decrease in clear sky OLR. Otherwise, the profile of precipitable water was found to be a dependent variable which was influenced by both thermodynamic and dynamic processes.

ACKNOWLEDGEMENTS

I wish to thank all of the people at CIRA and CSU for your assistance in helping me to compose this thesis and achieve my Masters Degree. In one way or another, you have all contributed to my education and this research. The generous sharing of your time, even when you were terribly busy, has helped me climb one step higher in the lifelong pursuit of knowledge and wisdom.

In particular, I would like to thank Tom Vonder Haar for first welcoming me into the department. Your confidence and support has been greatly appreciated, and I have striven to make a positive contribution. Thank you also to Dave Randel who helped me to get through the day-to-day trials of graduate and research life. I am most grateful for your open door and helpful advice, especially in times of crisis.

My thanks are also extended to the many computer-friendly people at CIRA. Nan McClurg, Ian Wittmeyer, Duane Whitcomb, Kelly Dean, Garrett Campbell, and Mike Hiatt have provided me with valuable computer assistance. Time and time again, they walked me through the maze of computational nightmares in which I found myself. Loretta Wilson and Joanne DiVico have helped me overcome administrative hurdles. Thank you.

My fellow graduate students deserve a debt of gratitude. Your friendship, wit, and criticism carried me a long way. Thanks especially to Andy Jones and Harold Gibson for your insights.

Most importantly, thank you goes to my dear wife Peggy. Without your constant love and support, I never would have survived this truly challenging and amazing experience. May you help me to survive many more...

This work has been supported by NASA Grant NAGW-2700.

TABLE OF CONTENTS

LIST OF TABLES

LIST OF FIGURES

Chapter 1

INTRODUCTION

Water vapor is the principal greenhouse gas and plays a major role in the overall energy balance of the atmosphere. Water vapor regulates the energy balance through selective absorption and transmission of solar and terrestrial radiation. Water vapor intercepts a broad band of infrared radiation emitted by the surface and subsequently emits it at lower temperatures.

One measure of the water vapor content of the atmosphere is precipitable water, expressed as the depth to which water would stand if the vapor in a unit area column of air were condensed. Precipitable water is defined as the vertical integral of the mean specific humidity,

$$\overline{W} = \int_{p_1}^{p_2} \overline{q} \, \frac{dp}{g}.$$

The characterization of global moisture fields advanced with the establishment of the synoptic radiosonde network after World War II. Early research sought to produce basic climatologies of water vapor distribution. Recent research has concentrated on the role of water vapor in the global energy balance, specifically the area of global climate change. An historical summary of various researchers efforts in the field of precipitable water studies is presented below.

Bannon, *et al.* (1960) presented global charts depicting the mass of water vapor above one square centimeter at the earth's surface and above each of the levels 850, 700, and 500 hPa. Over land, the charts showed moisture structure coinciding with topography and seasonal circulations. Over data-sparse regions such as oceans and the former Soviet

Union, moisture fields were quite smooth. It was found that water vapor was a maximum over land in the summer and was associated with temperature distribution.

Reitan (1960) presented the distribution of precipitable water over the United States from mean monthly radiosonde data for an eleven year period. The general latitudinal decrease of precipitable water toward the north and small mean values over higher terrain were identified. Average precipitable water content over the United States was determined to be 1.71 cm. Monthly patterns between October and March showed little change in form and features, exhibiting low values over the West and a large gradient near the Gulf coast gradually decreasing toward the northern border. From April to July, patterns showed a noticeable increase in precipitable water over the central and eastern United States. A gradual movement of moisture into the Southwest during July and August was also apparent.

Peixoto, *et al.* (1981), using homogeneous data from the International Geophysical Year, explored intra-annual variations in mean precipitable water over the northern hemisphere and found general zonal symmetry and monotonic decrease from equator to pole. This decrease resulted from the temperature dependence in the atmosphere's ability to retain water vapor, the Clausius-Clapeyron relationship,

$$e_s = e_{s_0} \exp\left[\frac{L}{R_v}\left(\frac{1}{T_0} - \frac{1}{T}\right)\right]$$

in which the saturation vapor pressure varies with temperature. Departures from zonal symmetry were noted to be associated with the nature of the underlying surface. Moisture contents were thus typically higher over the oceans than the continents, especially near tropical and subtropical coastal regions. Minima occurred above high terrain and over deserts where subsidence prevails. Seasonal variations were generally found to be consistent with the variation in temperature during the year and were more marked over land than over the oceans. Large seasonal differences occurred in connection with the

Indian and southeast Asian monsoons. The high thermal inertia of the ocean was identified in the generally moister conditions in October than April.

Trenberth, *et al.* (1987), examined water vapor variations through its effects on surface pressures. At the time, direct measurements of global water vapor content were difficult and lacked observations over the open oceans. Thus, the alternative approach was to assess the changes in total water vapor by measuring its effects on surface pressures. The hypothesis was that all variations in global surface pressures should be due to changes in water vapor content. Surface pressures due to water vapor were computed using,

$$P_w = \int_{ps}^{P_t} q \, dp,$$

differing from the total precipitable water by a factor of g. The annual water vapor cycle resulted in a global mean surface pressure range of ~0.4 hPa. Water vapor surface pressure had maximum annual mean values at the equator and monotonically decreased towards higher latitudes. At almost all latitudes, values were lower in the southern hemisphere than the northern hemisphere. With its greater land mass and continentality, the northern hemisphere showed a large annual temperature cycle and thus a larger annual water vapor cycle than the southern hemisphere. Changes in water vapor content also corresponded to interannual variability and trends in the total mass of the atmosphere related to such phenomena as the El Niño/Southern Oscillation.

Wittmeyer (1990), used TOVS total precipitable water content fields in determining poleward moisture transport over a study period of five years. A global monthly average of precipitable water content for September 1987 showed maxima along the Intertropical Convergence Zone, minima over high latitude land areas and elevated terrain, and gradients near continental margins. High values in the tropical eastern Pacific were linked to the large evaporation rates from the warm ocean surfaces there. Low land areas exhibited lower values than oceans at similar latitudes. The absolute global minima occurred over Antarctica at the end of a cold, dry winter.

Finally, Peixoto and Oort (1992) presented global mean precipitable water fields derived from global radiosonde observations which showed a continuous decrease from the equatorial regions to the poles. Departures from zonal symmetry arose from differences in the physiography of the earth's surface. Deflections of isolines near east and west coasts of continents were due to ocean current circulations. Areas drier than the zonal average included the deserts due to strong subsidence and mountain areas due to the high terrain. The January minus July difference showed the largest annual variations occur in relatively low latitudes over the continents, and variations associated with the Asian monsoons were very pronounced.

Because of their global viewing perspective, satellite observations of precipitable water can provide the quantitative measurements necessary for comprehensive studies of the earth's hydrologic cycle. Satellites and radiosondes differ in their method of retrieving water vapor profiles. While radiosonde measurements are directly determined by simple integration of observations, satellites sense the average state of a given atmospheric volume via passive observation of atmospheric emissions (Wittmeyer and Vonder Haar, 1991).

This study used blended radiosonde and satellite precipitable water data to examine distribution and interannual variability. Satellite and radiosonde measurements were merged to produce estimates of total column-integrated precipitable water, as well as a three-layer, vertical distribution of precipitable water at a one degree horizontal resolution (Vonder Haar, *et al.*, 1994; Randel, *et al.*, 1992). This merged dataset for the first time provides daily estimates of precipitable water on a global scale and offers many new research opportunities. The high resolution data is useful for investigating regional distributions of water vapor, as was done in this study. With continued processing of this data, a comprehensive water vapor climatology can be achieved. The three-layer data will be of particular use in future water vapor transport studies.

The merged precipitable water dataset was used in this research for three different studies. The first study assessed the monthly distribution and variability of precipitable water over the United States for 1988.

The second study examined interannual variability by comparing differences of monthly averaged precipitable water between 1988 and 1989. This study was chosen to search for evidence in the precipitable water fields of the great North American drought which occurred during the summer of 1988.

The final study evaluated the role of water vapor in the longwave radiative balance of the atmosphere. The merged precipitable water data was combined with ECMWF temperature analyses to investigate their relationships with clear sky outgoing longwave radiation over land. Previous research has mainly concentrated on the longwave radiative effects of water vapor over the oceans and in low-latitudes where conditions vary slowly on a spatial and temporal scale. The analysis was facilitated with the use of a radiative transfer model supplied with observations of surface and atmospheric temperatures, as well as three-layer precipitable water data.

Chapter 2

WATER VAPOR DISTRIBUTION AND VARIABILITY

Water vapor is the principal greenhouse gas and plays a major role in the overall energy balance of the atmosphere. Water vapor regulates the energy balance through selective absorption and transmission of solar and terrestrial radiation. One measure of the water vapor content of the atmosphere is precipitable water, expressed as the depth to which water would stand if the vapor in a unit area column of air were condensed. Precipitable water in a layer is defined as the vertical integral of the mean specific humidity in that layer,

$$\overline{W} = \int_{p_1}^{p_2} \overline{q} \, \frac{dp}{g}.$$

In this first study, the distribution and variability of monthly averaged precipitable water were assessed. Data used were for January, April, July, and October of 1988 which were representative of the four mid-latitude seasons.

2.1 PRECIPITABLE WATER MEASUREMENTS

The merged precipitable water dataset used in this study was produced from global radiosonde and satellite observations for the National Aeronautics and Space Administration (NASA).

Carried aboard the NOAA polar orbiting satellites is the TIROS Operational Vertical Sounder (TOVS) instrument package for retrieval of atmospheric temperature, ozone, and water content. The TOVS system is made up of the second generation High Resolution Infrared Radiation Sounder (HIRS/2), the Microwave Sounding Unit (MSU), and the

Stratospheric Sounding Unit (SSU). The HIRS/2 and MSU are used for retrieval of vertical moisture profiles. The individual scan spot data from the HIRS/2, MSU, and SSU is processed to convert 27 channel radiances to vertical profiles of temperature, water content, and ozone. The TOVS processing system is operated by the National Environmental Satellite, Data, and Information Service (NESDIS). Because HIRS/2 moisture channels sense radiation in water vapor absorption bands, these channels cannot be used under cloudy scene conditions due to the opaque nature of clouds at these wavelengths (Wittmeyer, 1990). Daily TOVS sounding data is a composite of approximately 22,00 retrievals collected throughout a 24 hour period.

The Special Sensor Microwave/Imager (SSM/I) was launched as part of the United States Defense Meteorological Satellite Program (DMSP). This millimeter-wave radiometer measures thermal radiation from the earth's atmosphere and surface in four spectral bands of the 19-86 GHz domain. The radiation in all SSM/I channels is subject to atmospheric water vapor absorption and can be used separately or together to estimate the vertically integrated water vapor (Schluessel and Emery, 1990). Water vapor retrievals from SSM/I instruments are based upon the methodology of Greenwald, *et al.* (1993) using observations from the 19.35 and 37 GHz channels. This method involves the depolarization of the radiation emitted and reflected by the ocean surface by atmospheric constituents, mainly water vapor and liquid water, on its transfer to the satellite sensor. SSM/I water vapor retrievals are not available over land due to the high variability of surface emissivity.

With data from the global radiosonde network which has undergone climatological quality control (Elliot, *et al.*, 1994), the TOVS and SSM/I data are blended into a global set of daily averaged, column-integrated and layered precipitable water with horizontal resolution of one degree (Vonder Haar, *et al.*, 1994). The precipitable water product represents a weighted merge of SSM/I microwave retrievals, TOVS infrared retrievals, and radiosonde data using a hierarchical weighting scheme. This merging process draws upon

the strengths of each of the retrieval methods to produce a comprehensive precipitable water dataset that is better than any one single dataset. The algorithm uses radiosonde data when available as truth, and then applies a weighting scheme to the TOVS and SSM/I data. Linear and temporal interpolation routines are run to fill missing data points.

The layered product was developed using level information contained in the TOVS and radiosonde data. TOVS precipitable water retrievals are reported at three layers: surface to 700 hPa, 700 to 500 hPa, and 500 to 300 hPa. The global radiosonde retrievals are divided to match these same layers. The SSM/I does not provide level information. For each day, three global grids are formed as the percent-of-total precipitable water content in each of the three layers. Spatial and temporal interpolations are used to fill in missing data points. The assumption used in this method is that while the total and layered precipitable water content can change rapidly, the percent-of-total in each layer is much more stable. The variability in the percent-of-total is a strong function of latitude and season and does not vary spatially as fast as the precipitable water content itself. These percent-of-total fields are multiplied by the total precipitable water contents created in the merge process and output as layered precipitable water content global grids.

Precipitable water data are available globally for the 1988-1989 period. This study was restricted to a regional scale centered over the United States.

2.2 MONTHLY DISTRIBUTION OF PRECIPITABLE WATER

In the first part of this study, monthly averages of column-integrated precipitable water over the United States were calculated from the daily fields. These averages are presented in Figures 2.1 through 2.4 for January, April, July, and October of 1988 which represent the mid-latitude seasons. All of the monthly averages showed a general decrease of precipitable water from low to high latitudes. This emphasized the general dependence of average precipitable water to average temperature which also monotonically decreases with

Figure 2.2. Average column-integrated precipitable water for April 1988 in millimeters.

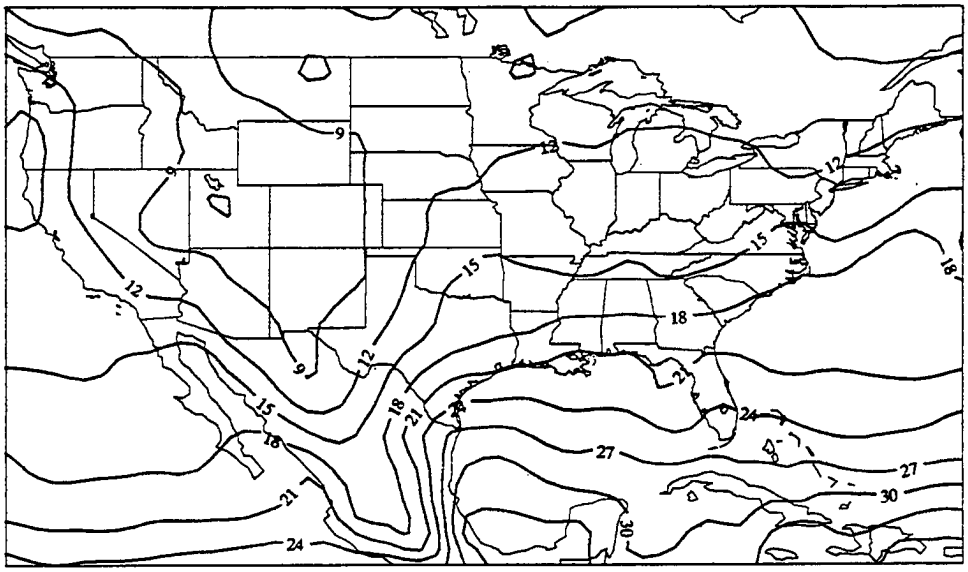

The precipitable water over the rest of the area in April shows a similar structure to that of January, but with average values a few millimeters greater.

The 18 mm isoline has the same general shape as in January, except that its location has shifted farther to the north. It still mainly runs west to east from the Pacific Ocean to the Atlantic Ocean, except for its southern deflection across Mexico due to the Mexican highlands. The line parallels the Gulf Coast of the United States once again, but its position is inland in April.

Comparison with Reitan's results showed similar distributions of precipitable water for April. The minima over the Rockies were almost identical between the two studies. Once again, the position of the 18 mm isoline was farther north in Reitan, stretching across the middle Atlantic states with the southeastern and middle Atlantic states higher overall by two to five mm. Reitan also indicated values of 15 to 16 mm of precipitable water over the west coast of the United States where the present study had values closer to 12 to 13 mm.

For July, the minima are again found over the high mountain terrain, while the maxima are found over the Caribbean Sea and Gulf of California. July values represent the annual maxima in precipitable water for most areas over the United States. The summer monsoonal flow over the Southwest, with the general circulation transporting air northward from the Gulf of California and the Pacific Ocean, is responsible for the intrusion of high values of precipitable water over this region. The large values over the eastern half of the United States are the result of the warm, moist flow of air from the Gulf of Mexico in the summertime circulating around the semi-permanent Bermuda high pressure system. Land-sea contrasts are most pronounced over Mexico where the Mexican highlands are sandwiched between the Pacific Ocean and Gulf of California to the west and the Gulf of Mexico to the east.

The warm average July temperatures allow for the 18 mm isoline to be found well to the north and west of its winter and spring positions. Its position is located in the dry intermountain west of the United States and stretches northwestward into western Canada.

Figure 2.3. Average column-integrated precipitable water for July 1988 in millimeters.

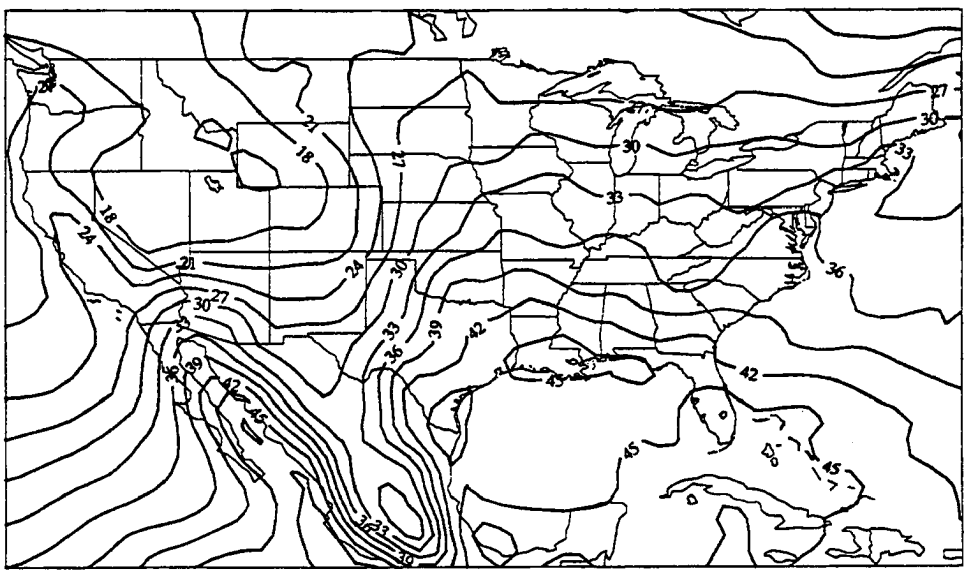

The present study showed considerably more detail in the precipitable water field for July than indicated in Reitan's analysis. The large gradients in precipitable water due to the land/sea contrasts between the southwestern United States, Baja, and Mexico and the Pacific Ocean, Gulf of California, and Gulf of Mexico were not captured in Reitan's study. However, the position of the 18 mm isoline was nearly identical between the two studies.

As with April, October marks a transition between seasons, from summer to winter. Because of thermal inertia from summer, precipitable water values in October are higher than those in April. The southern states and the Gulf of Mexico exhibit the highest values of precipitable water as average surface conditions are still warm at this time of year. The minima are found over the highest terrain and the northern states cut off from ocean influences. The gradient of precipitable water and deflection of the contours to the north is quite pronounced off the eastern coast of the United States as cooler continental air competes with the warm moist air over the Gulf Stream and Caribbean Sea.

The thermal lag between summer and autumn in the northern hemisphere allows for the 18 mm isoline to be positioned farther north in October than it was in April. The isoline mainly runs west to east across the southern United States. However, the line is deflected south when it encounters the elevated terrain of the southern Rocky Mountains. It is then deflected back toward the north over the southern plains due to the influence of the Gulf of Mexico before it continues east-northeastward over the Atlantic Ocean.

The comparison between the present study and Reitan for October continued to show similar features. Both studies captured the minima found in the central Rocky Mountains with maxima located over the Gulf of Mexico. As in previous months, Reitan's values of precipitable water were higher over the southeastern and middle Atlantic states than in the present study by approximately five mm. The position of the 18 mm isoline was well to the north in Reitan's analysis stretching eastward across the central Great Plains and into the northern middle Atlantic States.

Figure 2.4. Average column-integrated precipitable water for October 1988 in millimeters.

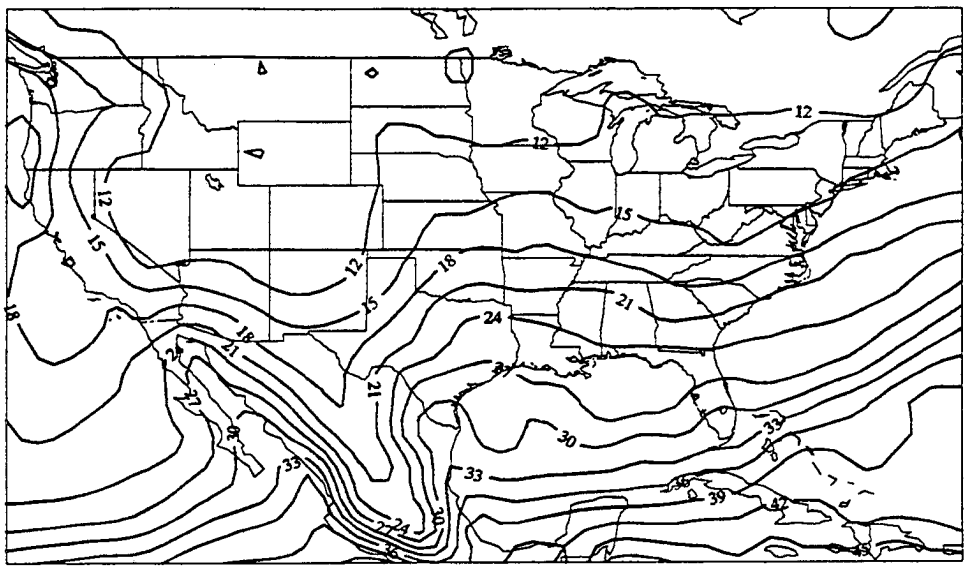

2.3 MONTHLY VARIABILITY OF PRECIPITABLE WATER

In the second part of this study, the coefficient of variation was used to examine the relative variability of precipitable water over a month. The coefficient of variation is a normalized quantity and is defined as the ratio of the standard deviation to the monthly mean and is expressed as a percentage. It is useful to normalize the standard deviation by the mean to minimize the regional variations in average precipitable water content. Figures 2.5 through 2.8 show the coefficients of variation for January, April, July, and October of 1988.

For January, the largest variations are located off the eastern coast of the United States. These are due to the sharp land-sea contrasts between the cooler, drier continental air and the warmer, moister maritime air over the Gulf Stream. The variability arises from continental air flow off the East Coast competing with maritime air flow associated with cyclogenesis along the Gulf Stream. High variations found over the Rocky Mountains and over the northern states are the result of small changes in precipitable water occurring in areas where the monthly means are already quite small. Smallest variations are found over the Caribbean Sea where warm, stable conditions exist.

Conditions during April are quite uniform, with coefficients of variations near 30% over most of the area. The highest values over the Mexican Plateau and western Texas are most likely associated with the resurgence of low-level southerly moist flow from the Gulf of Mexico which occurs in the springtime. Lowest variations are found over the stable regions of the Caribbean and the stratocumulus regions to the west of the Baja peninsula.

July is representative of the low variability in precipitable water found during the summer months. July variations are much less than January as a result of higher average values of precipitable water and weaker, less frequent travelling wave activity. The high areas shown reflect the influences of easterly waves moving across central Mexico, the

land-sea contrasts off the East Coast of the United States, and the variability in stratocumulus cloudiness off the California coast.

With the transition from summer to winter, variations shown in October represent the clash of the seasons across the northeastern United States Surges of cooler and drier air from the north and west invade areas where warm, moist conditions have lingered from summer. Stable conditions and relatively slow changes from summer to winter across the rest of the United States result in low variations between 20% and 30%.

Figure 2.5. Coefficient of variation of precipitable water for January 1988 in percent.

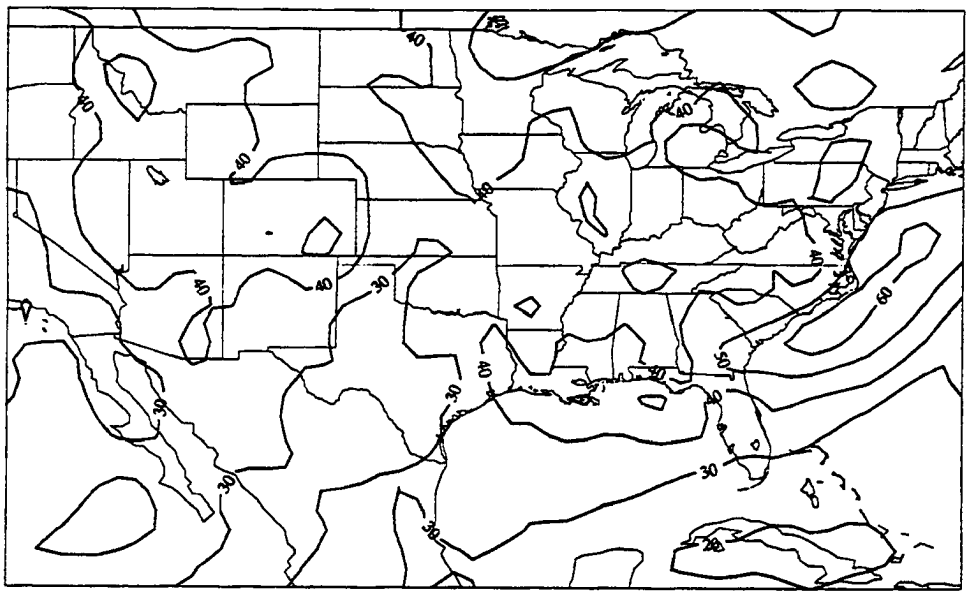

Figure 2.6. Coefficient of variation of precipitable water for April 1988 in percent.

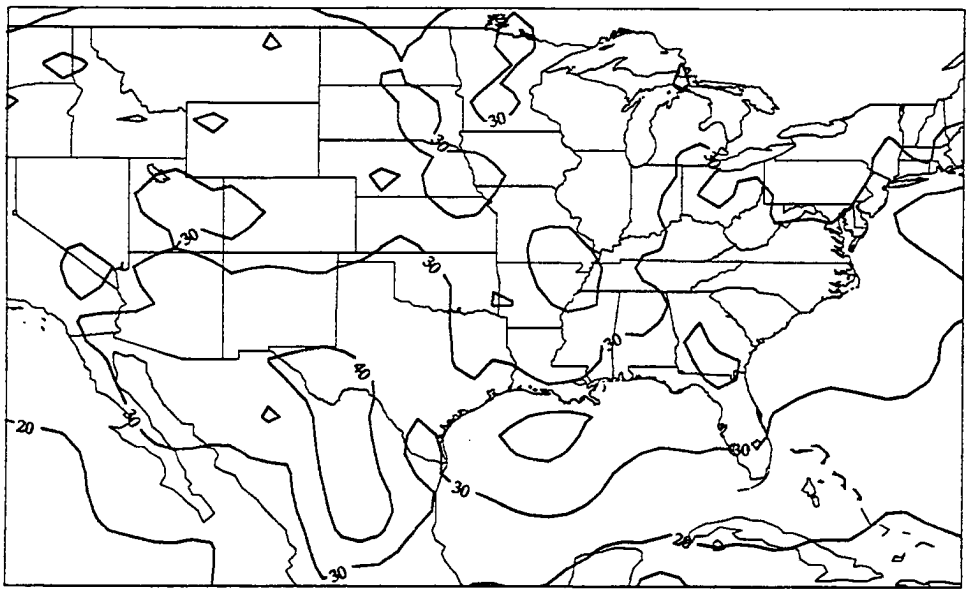

Figure 2.7. Coefficient of variation of precipitable water for July 1988 in percent.

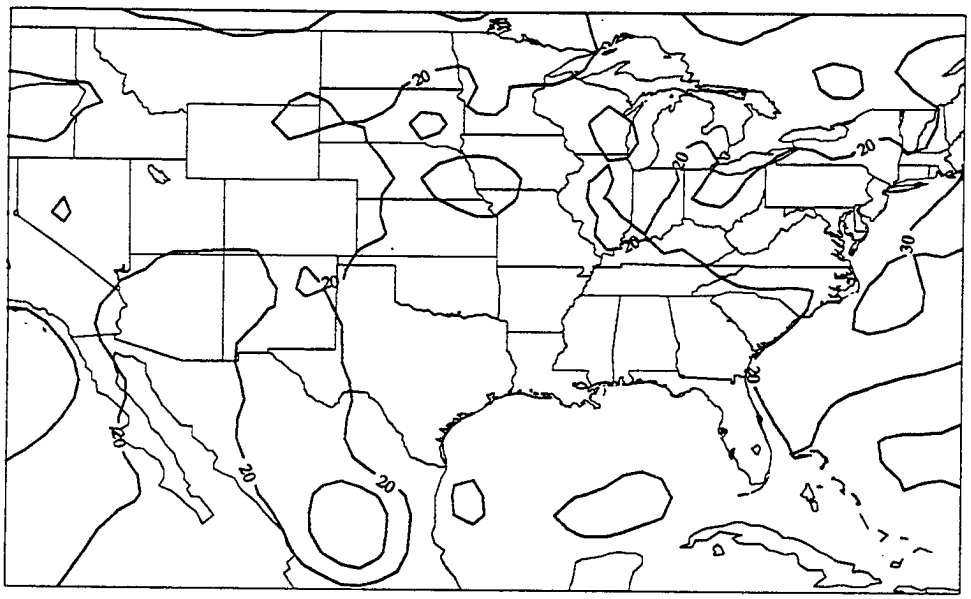

Figure 2.8. Coefficient of variation of precipitable water for October 1988 in percent.

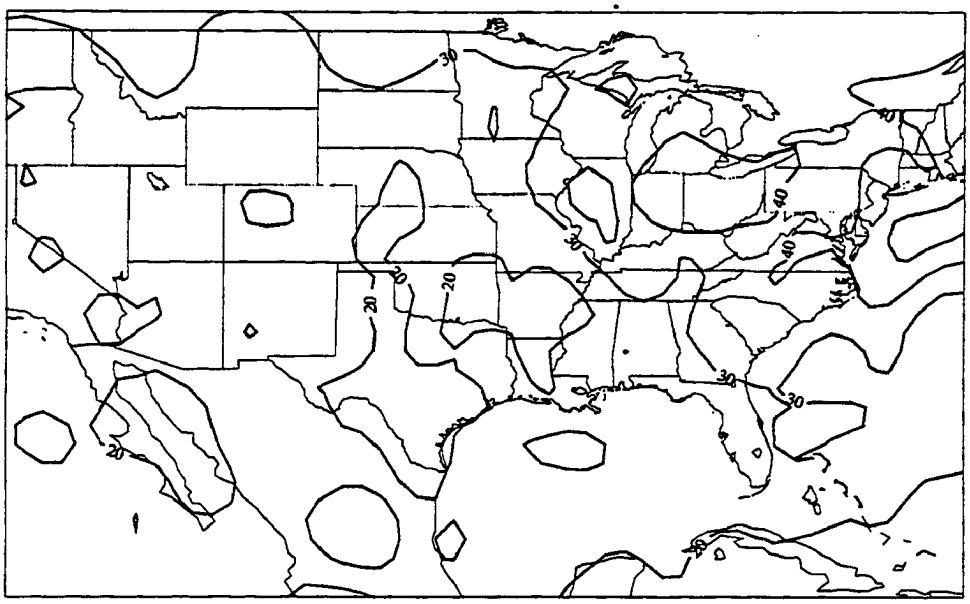

2.4 1988 NORTH AMERICAN DROUGHT

The 1988 summer drought in the United States was the most extensive in many years. As a whole, the United States was the driest on record since at least 1895 when record-keeping began (Trenberth and Branstator, 1992). The most severely stricken regions of the Great Plains, Midwest, and lower Mississippi Valley had record low rainfalls between April and June 1988. By July 1988, 43% of the area of the United States was in the severe or extreme drought category (Trenberth, *et al.*, 1988). Yet droughts are regularly occurring phenomena and are part of natural variations in the climate system.

What was the cause of the drought? The 1988 drought developed at different times and places across the country. These regional events cannot be traced to the same cause. Trenberth and Branstator (1992) and Trenberth, *et al.* (1988) suggested the primary cause of the drought was a change in the atmospheric circulation across North America brought about as a teleconnection forced by changes in sea surface temperatures (SSTs) in the tropical Pacific. Tropical SST changes are reflected in the atmosphere through changes in the location of convergence zones, rainfall, and latent heating. Beginning in April, and continuing through May and June of 1988, the atmospheric circulation was observed to change to strongly anticyclonic conditions in the upper troposphere centered over North America, displacing the jet stream and associated storm tracks well north of normal. In addition, this anomalous anticyclonic circulation shut off the Midwest from its main source of moisture, the Gulf of Mexico. The northwesterly anticyclonic flow found over the Midwest inhibited Gulf moisture from penetrating this region. The normal southerly air flow found on the western side of the anticyclone was displaced farther west resulting in an early and enhanced monsoon flow in the southwestern United States (Trenberth, *et al.*, 1988).

The jet stream and circulation pattern associated with the strong upper-level anticyclone that led to the April through June drought broke down in early July. From then

on precipitation returned to much closer to or even above normal in areas substantially affected by the drought. However, the normal precipitation experienced in July and August 1988 was not enough to break the hydrological drought which was maintained by continuing strong evapotranspiration.

Water vapor fields for the spring and summer of 1988 and 1989 were examined to search for a link between precipitable water and drought conditions. The goal was to determine if monthly averaged precipitable water was less for 1988 than 1989. Difference maps were produced by subtracting monthly averaged precipitable water for 1988 from monthly averaged precipitable water for 1989. Difference maps are presented for the spring and summer of 1988 versus 1989 in Figures 2.9 through 2.14.

March of 1989 showed considerably more water vapor over the southern half of the United States than in 1988. Yet, over the Gulf of Mexico, the Mexican States, and stretching westward into the Pacific Ocean, substantially drier conditions were found in 1989.

April 1988 versus April 1989 showed a similar pattern to that of March, but the differences between the two years were much less pronounced. The southern United States and Gulf Coast states showed an average of two millimeters less precipitable water in 1988 than 1989.

In May, areas over the central Gulf Coast showed a 1989 precipitable water excess of six millimeters over 1988 conditions. A small pocket where 1988 was moister than 1989 was found over the northern Great Plains. The May difference map shows some indication of the anomalous anticyclonic circulation over the Midwest. The lower precipitable water contents of the Gulf Coast region signal the cut off of moisture from the Gulf of Mexico due to the northwesterly flow found to the north.

June showed the most striking contrasts between years. The entire East Coast and the Gulf of Mexico was drier in 1988 than 1989—as much as 10 mm along the Virginia coastline. However, the northwestern Great Plains and central Mexico had considerably

more precipitable water in 1988 than in 1989. June marked the height of the 1988 drought in the midwestern United States, and the cutoff from Gulf moisture still seemed to be evident in the Midwest.

By July, the differences were relatively small over the entire United States The greatest contrast was found over southern Texas and central Mexico where 1988 precipitable water exceeded 1989 by six millimeters. In July 1988, the synoptic anticyclonic conditions maintaining the drought had begun to break down.

August showed negative differences stretching from the southern California coast, across the southern half of the United States, and into the upper Midwest and Northeast.

Overall, the comparison between years did not support an overwhelming, continued deficit in precipitable water during the entire spring and summer of 1988. The general circulation limited the ability of the Gulf of Mexico to provide moisture to the Midwest during May and June of 1988, yet precipitable water was still available over this region. Thus, precipitable water does not necessarily guarantee rainfall. Favorable atmospheric dynamics are required to initiate rainfall from otherwise vapor-laden skies.

One limitation in this comparison was the availability of only two years of data. With an increased archive of precipitable water data, the 1988 drought signal may become more evident against longer term monthly averages. This comparison between 1988 and 1989 did more to reveal the different monthly synoptic conditions than long-term climatological differences.

Figure 2.9. March 1989 minus March 1988 precipitable water difference in millimeters.

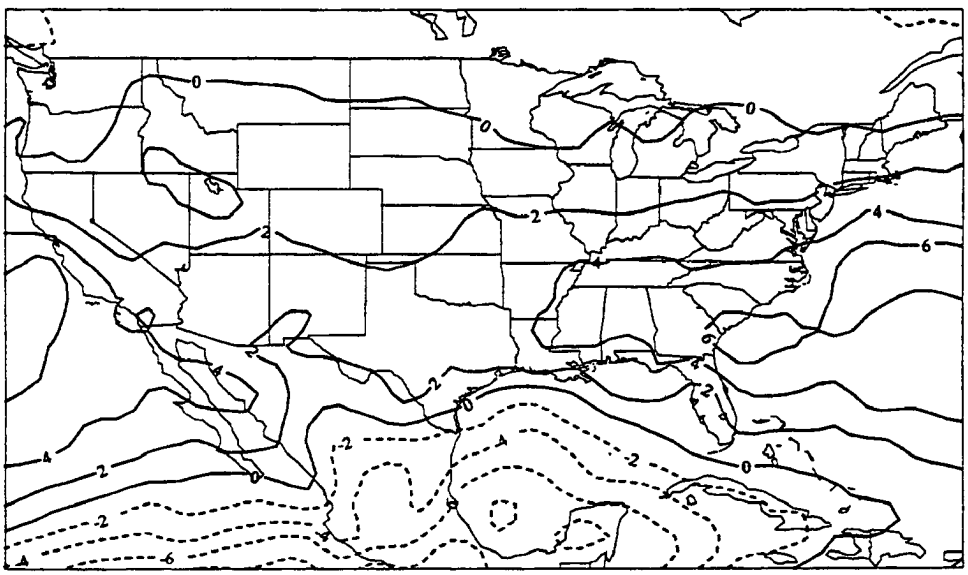

Figure 2.10. April 1989 minus April 1988 precipitable water difference in millimeters.

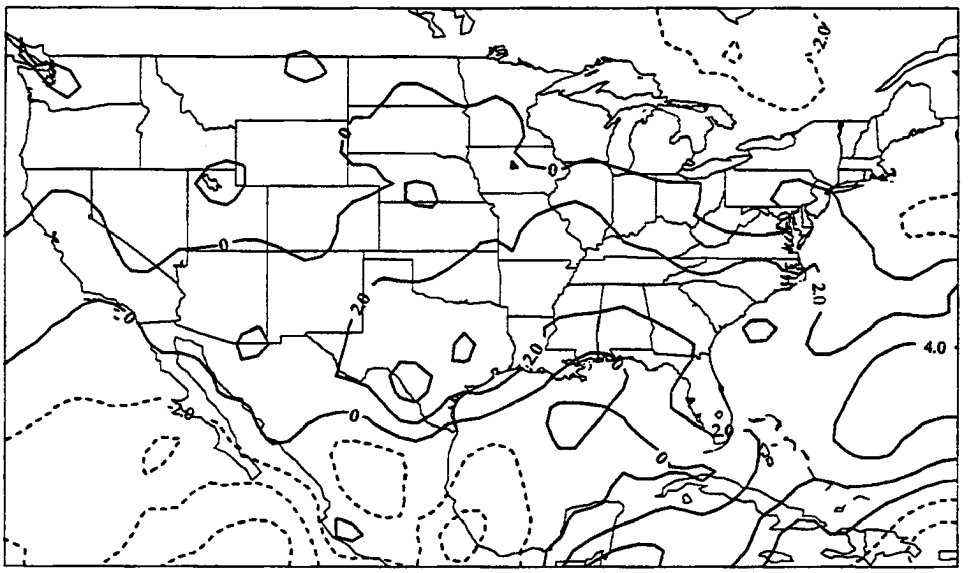

Figure 2.11. May 1989 minus May 1988 precipitable water difference in millimeters.

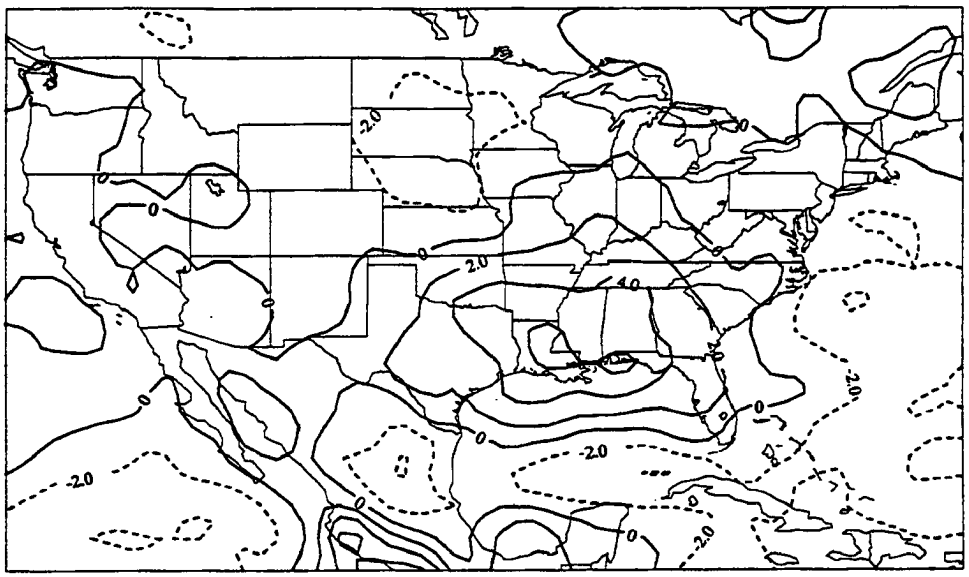

Figure 2.12. June 1989 minus June 1988 precipitable water difference in millimeters.

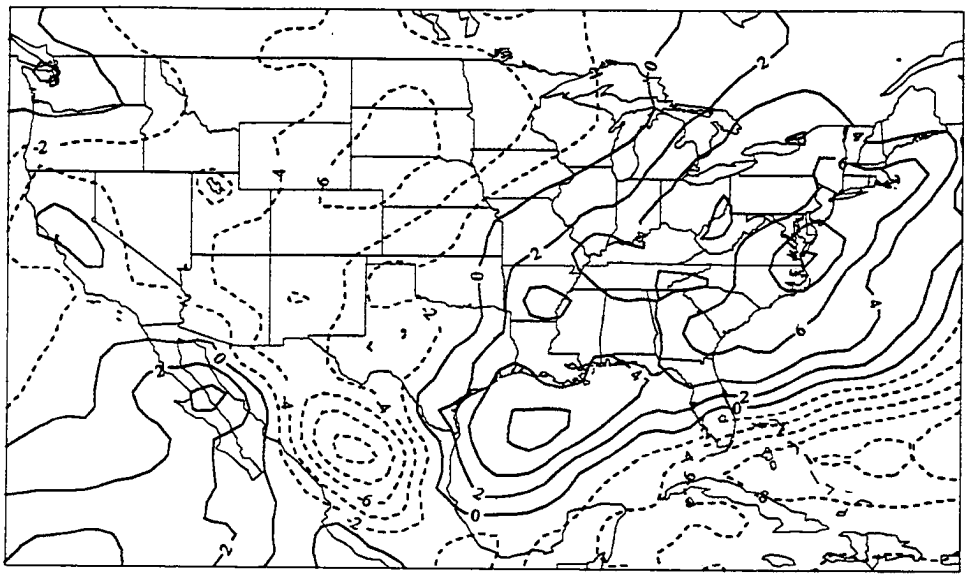

Figure 2.13. July 1989 minus July 1988 precipitable water difference in millimeters.

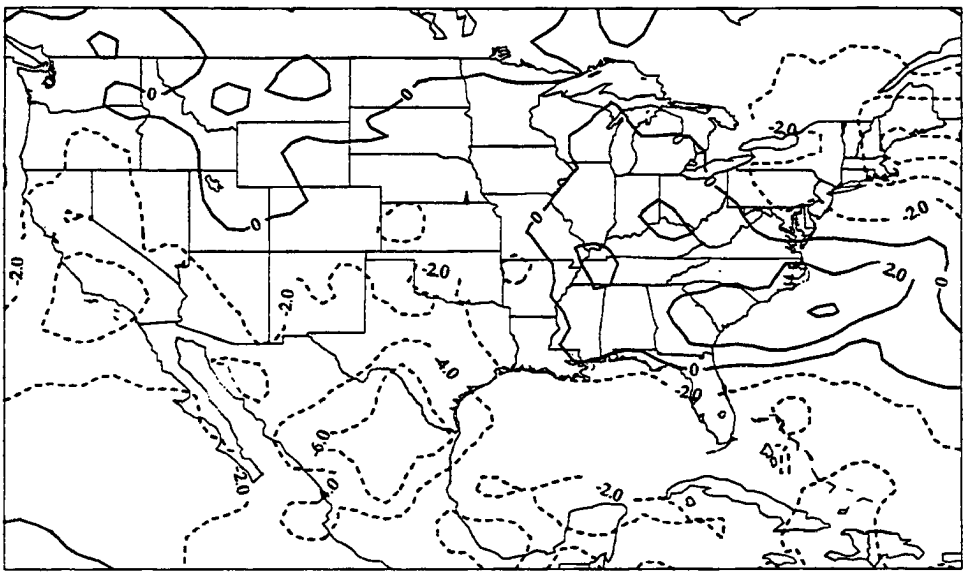

Figure 2.14. August 1989 minus August 1988 precipitable water difference in millimeters.

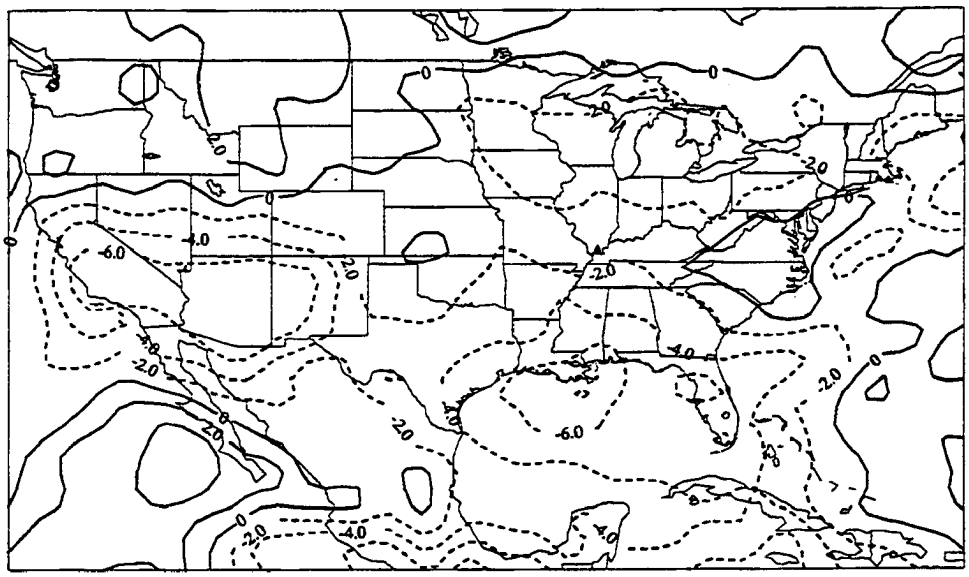

Chapter 3

CLEAR SKY OUTGOING LONGWAVE RADIATION

The second study in this research examined the radiative effects of water vapor on clear sky outgoing longwave radiation (OLR). Water vapor in a clear atmosphere selectively absorbs longwave radiation emitted at the earth's surface preventing its loss to space. Thus, for an increase in atmospheric water vapor there is a corresponding decrease in clear sky OLR at the top of the atmosphere. Previous studies have measured changes in water vapor associated with changes in sea surface temperature and how these together affect the clear sky outgoing longwave radiation. These studies will be discussed in Chapter 4.

3.1 CLEAR SKY OLR OVER LAND

Many land areas of earth exhibit regular diurnal variations in longwave radiation due to surface temperature fluctuations. Such behavior can easily be seen over cloud-free land, and is especially prominent over desert areas (Satran, *et al.*, 1986). To determine the sensitivity relationship of water vapor to clear sky OLR, daily fields of clear sky OLR are needed. The problem is that daily fields of clear sky OLR over land are not produced by the Earth Radiation Budget Experiment (ERBE) averaging system because of insufficient sampling of the diurnal cycle.

One of the original goals of NASA's Earth Radiation Budget Experiment was to determine of the diurnal variability in the earth's radiation balance (Brooks and Minnis, 1984). To accomplish this, a system of three satellites—one non-sunsynchronous ERBS spacecraft in a 57° orbit and two sun-synchronous NOAA polar orbiters—was designed to

most completely sample the diurnal cycle. Unfortunately, except for a three month period, ERBE narrow field-of-view scanner observations were available from only two satellites at a time—from ERBS and one NOAA polar orbiter. This arrangement typically provided only two to four observations per ERBE 2.5° region per 24 hours, even less for clear sky earth radiation budget measurements.

For this research, clear sky OLR measurements from satellite scanner data were utilized from the ERBE spatial averaging monthly archival tape (S-4) and the ERBE monthly archival tape (S-9) (Satran, *et al.*, 1986). The S-4 tape product is a single, monthly tape containing regional, zonal, and global spatial averages of the shortwave and longwave fields. The S-9 tapes include observations of each geographic region at the nearest local hour, as well as averages for each observed day and hour of the month, except for clear sky land conditions. In all cases, because of insufficient diurnal sampling, certain daily and hourly averages of clear sky data over land or desert are not produced by the ERBE averaging system for the S-9 archival tape.

The S-9 tapes were used to extract hourly data of clear sky OLR. These hourly data were interpolated using two different methods—one for land data and one for ocean data—to produce estimates of daily clear sky OLR. Monthly averages of these daily data were calculated and compared with the S-4 monthly averages produced by the ERBE system. The S-4 fields were used as "truth" values to test the accuracy of the interpolation methods.

Normally, values missing in the day-hour matrix were interpolated by the ERBE averaging system (Satran, *et al.*, 1986), using a half-sine model to represent the effects of diurnal surface heating in the case of clear sky conditions over land and linear interpolation for all other situations. The diurnal model used by the ERBE averaging system was not intended to provide an accurate representation of the diurnal variation over the course of one day (Cheruy, *et al.*, 1991b). Rather, the objective was to provide accurate monthly mean values to ± 5 W/m^2 on the regional scale and to arrive at a reasonable estimate of the monthly mean diurnal variation. Although specific accuracy goals were set for the monthly

mean values of the earth radiation budget components on different spatial scales, no explicit requirements were stated for either the daily mean values or the monthly mean diurnal variation.

Cheruy, *et al.* (1991a and 1991b) developed multiple regression formulas to compare the monthly mean longwave diurnal variations determined from ERBE observations with estimates based on Meteosat geosynchronous data. Limitations were found in the use of the ERBE half-sine model used to interpolate missing data over clear sky land and desert regions. Such interpolation models have the potential for introducing distortion when the time sampling is incomplete. The distortion of the longwave diurnal cycle would have been much reduced if the full three-satellite ERBE system had been operational. With an incomplete ERBE system, observations from Meteosat and other geostationary satellites can be of value if one is interested in the diurnal cycle of earth radiation budget components.

A basic objective of the International Satellite Cloud Climatology Program (ISCCP) has been to collect and analyze satellite radiance data from polar-orbiting and geostationary satellites to infer the global distribution of cloud radiative properties in order to improve the modelling of cloud effects on climate (Schiffer and Rossow, 1983). However, researchers have utilized ISCCP data to calculate outgoing longwave radiation and its diurnal variation. The advantage to using ISCCP data has been the fact that geostationary satellites can give much better time sampling—as often as every half hour—than the ERBE satellite arrangement.

Wu and Chang (1992) studied the use of ISCCP C1 products to produce monthly mean OLR fields. Comparison between the ISCCP product and OLR fields based on HIRS2 retrievals showed general agreement. Discrepancies over land were related to surface temperature differences, while discrepancies over the ocean were due to humidity differences.

Campbell, *et al.* (1990) considered the possibility of using ISCCP data to better interpolate between missing ERBE clear sky observations. This method was used to give estimates of the broad band diurnal variations which were less dependent upon the standardized ERBE diurnal models. For small scale locations in the midwestern United States, linear regressions were performed between ERBE and ISCCP narrow band fluxes. By applying the regressions only to local areas for short time periods (1 month), most of the true broad band variations were retained. This method produced better estimates of diurnal flux variations than relying on the limited ERBE local time samples alone. Comparisons of the ERBE data estimates alone with the ERBE filled with ISCCP data showed a close correspondence between the diurnal models used in ERBE analysis and the diurnal variation of the narrow band ISCCP observations.

For this study, the ISCCP data used were from the stage C2 products, namely three-hourly, monthly averaged surface temperatures sampled at the 10.7 μm wavelength. These ISCCP temperatures were estimates of the surface blackbody temperature in the atmospheric window and were not corrected for longwave surface emissivity.

Since OLR in clear sky regions is dependent on surface temperature, to a first approximation these temperatures were able to be converted to longwave fluxes using the Stefan-Boltzmann relationship. The surface fluxes were used to define the shape of the diurnal cycle over land to aid in producing daily averages of clear sky OLR from incomplete ERBE hourly data. Because these data are in the atmospheric window transparent to water vapor, the diurnal range of these data are greater than the diurnal cycle of broadband longwave flux. However, the interpolation scheme to be used adjusts the diurnal amplitude to that of observed clear sky OLR data.

The interpolation scheme used in this study can produce daily averages of clear sky OLR over land because it captures the diurnal cycle missed by the ERBE satellite system. The flowchart shown in Figure 3.1 demonstrates how the daily averages of clear sky OLR over land were produced.

Figure 3.1. Flowchart depicting the method used to interpolate missing ERBE hourly data points over land using ISCCP 10.7 μm monthly-averaged three-hourly surface temperatures.

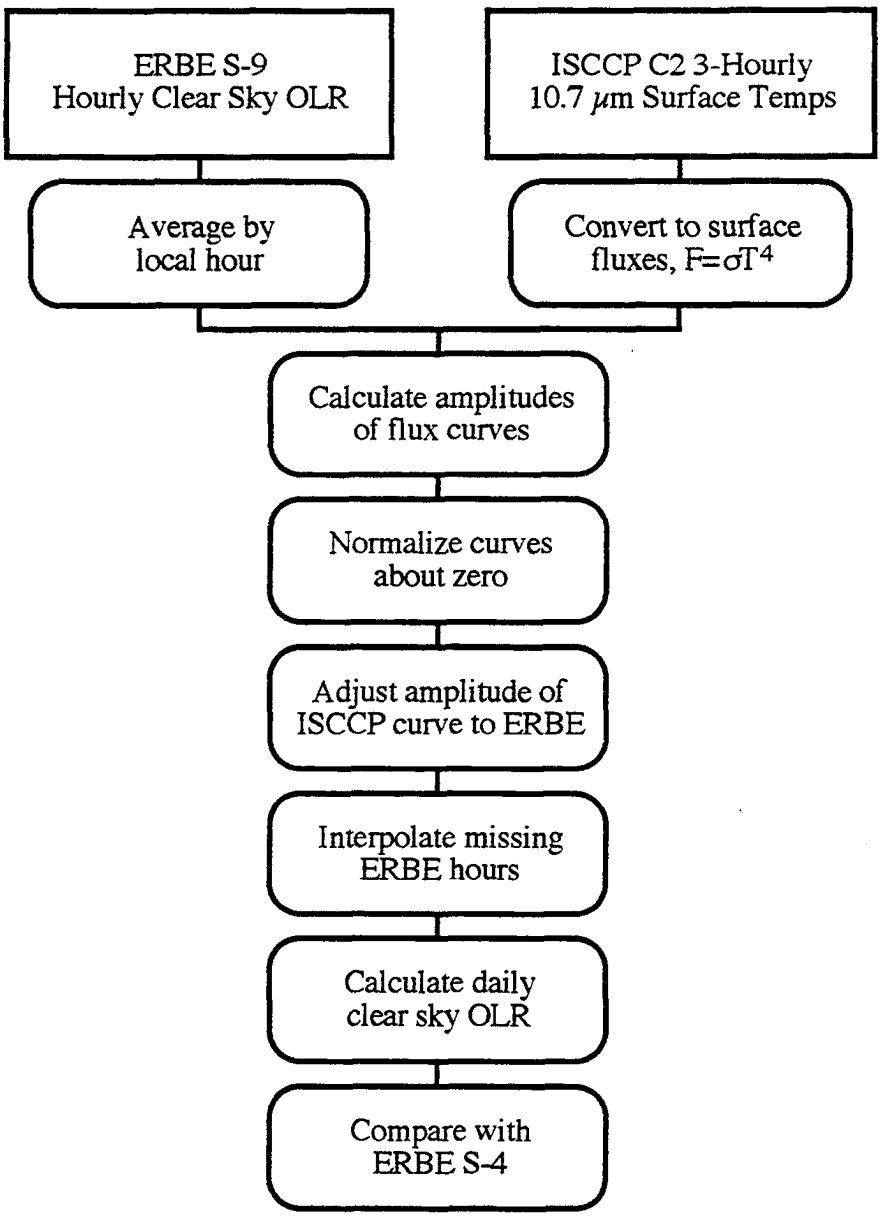

The ISCCP surface temperatures were converted to surface fluxes using $F=\sigma T^4$, where σ is the Stefan-Boltzmann constant. This represented the flux emitted from the surface at the 10.7 μm wavelength. A 24x31 matrix representing 24 hours per day and 31 days per month was filled with existing ERBE S-9 clear sky OLR data. An example of the distribution of hourly clear sky OLR data from ERBE S-9 measurements for July 1988 at the location 45° north latitude and 109° west longitude is presented in Figure 3.2. The available data was averaged by local hour. Figure 3.3 shows the flux curves from the ERBE S-9 and the ISCCP C2 data averaged by local hour. The amplitudes of both the averaged flux curves were calculated as the differences between the highest and lowest points on each curve. The flux curves were normalized about zero by subtracting one-half the amplitude from each curve. The normalized curves are shown in Figure 3.4. The amplitude of the ISCCP curve was adjusted to match the amplitude of the ERBE curve. A thorough analysis showed that the average amplitude of the ISCCP curve was approximately five times the amplitude of the ERBE curve. Thus, the amplitudes of the ISCCP curves were reduced by 80% in all cases as is depicted in Figure 3.5. One-half the amplitude was added back to each curve to return the curves to their original values. This is presented in Figure 3.6. Missing ERBE hourly data points were interpolated with coincident adjusted ISCCP data. Figure 3.7 shows three days of ERBE S-9 observations where missing ERBE hours were filled with adjusted ISCCP data. Daily averages of ERBE/ISCCP interpolated data were calculated for each location. Finally, monthly averages of the interpolated data were calculated and compared with ERBE S-4 monthly averaged data at each 2.5° grid location.

Comparison of monthly averages of clear sky OLR between ERBE S-4 and the interpolated ERBE/ISCCP product resulted in differences of generally less than five W/m^2 for each month in 1988. Recall that the original objective of the ERBE averaging system was to provide accurate monthly mean values to ±5 W/m^2 on a regional scale. Figure 3.8

Figure 3.2. ERBE S-9 clear sky OLR data distributed by local hour for July 1988.

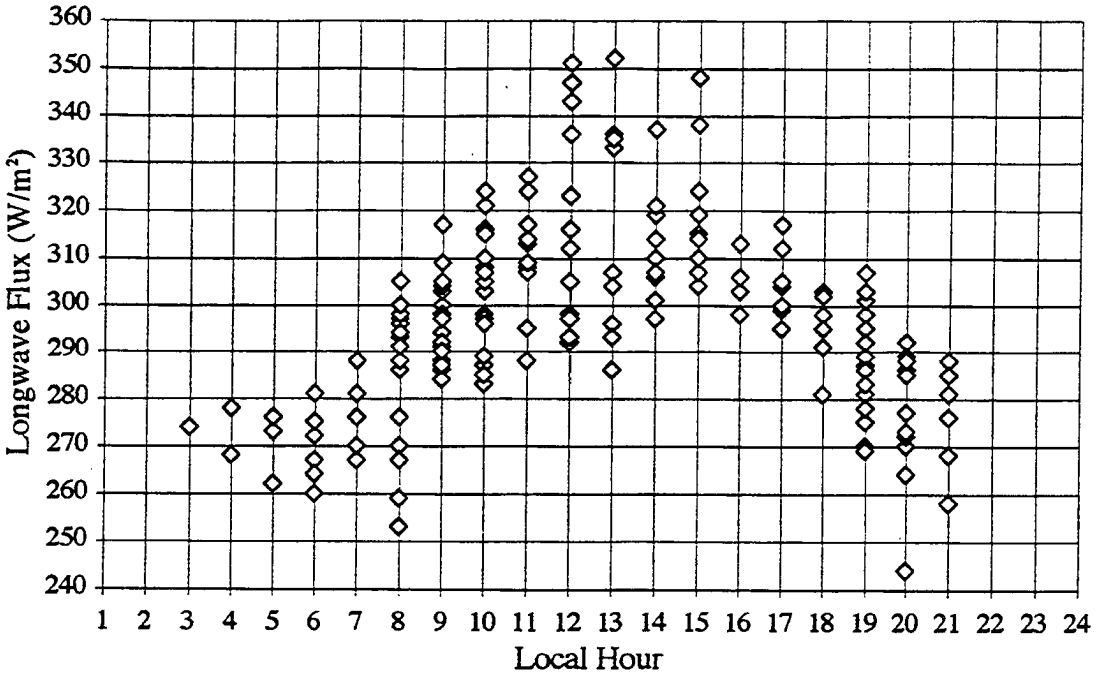

Figure 3.3. ERBE S-9 hourly averaged clear sky OLR data and ISCCP C2 three-hourly averaged surface fluxes computed from 10.7 μm surface temperatures for July 1988.

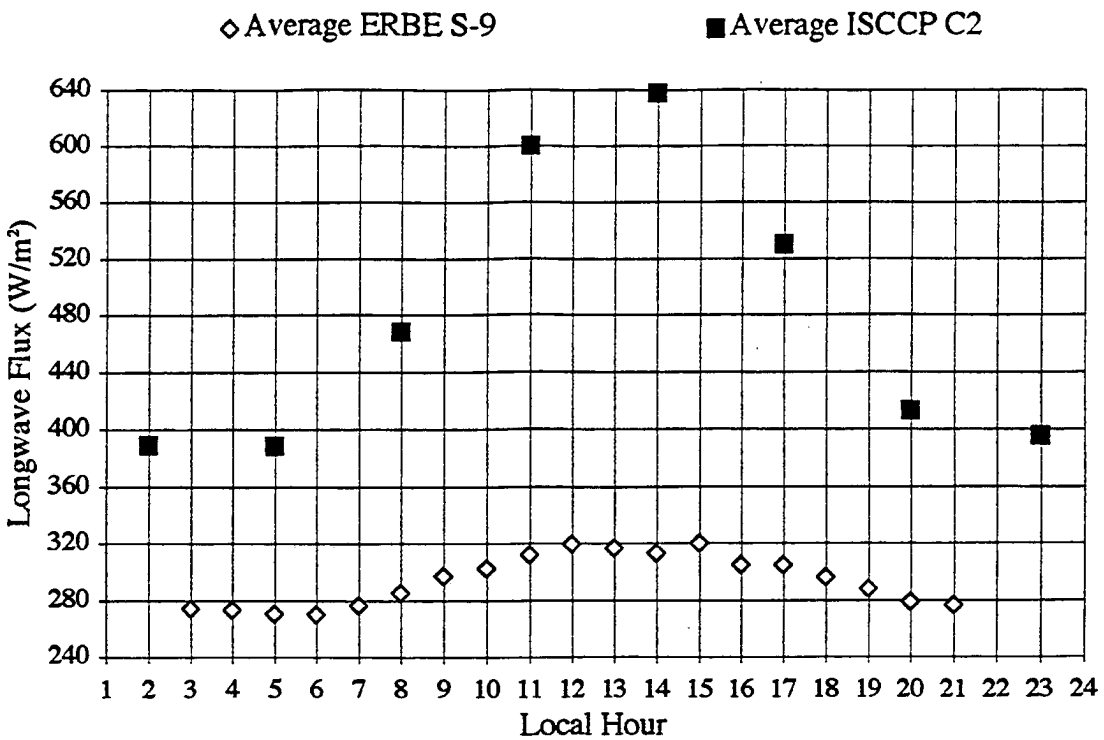

Figure 3.4. ERBE and ISCCP flux curves normalized about zero for July 1988.

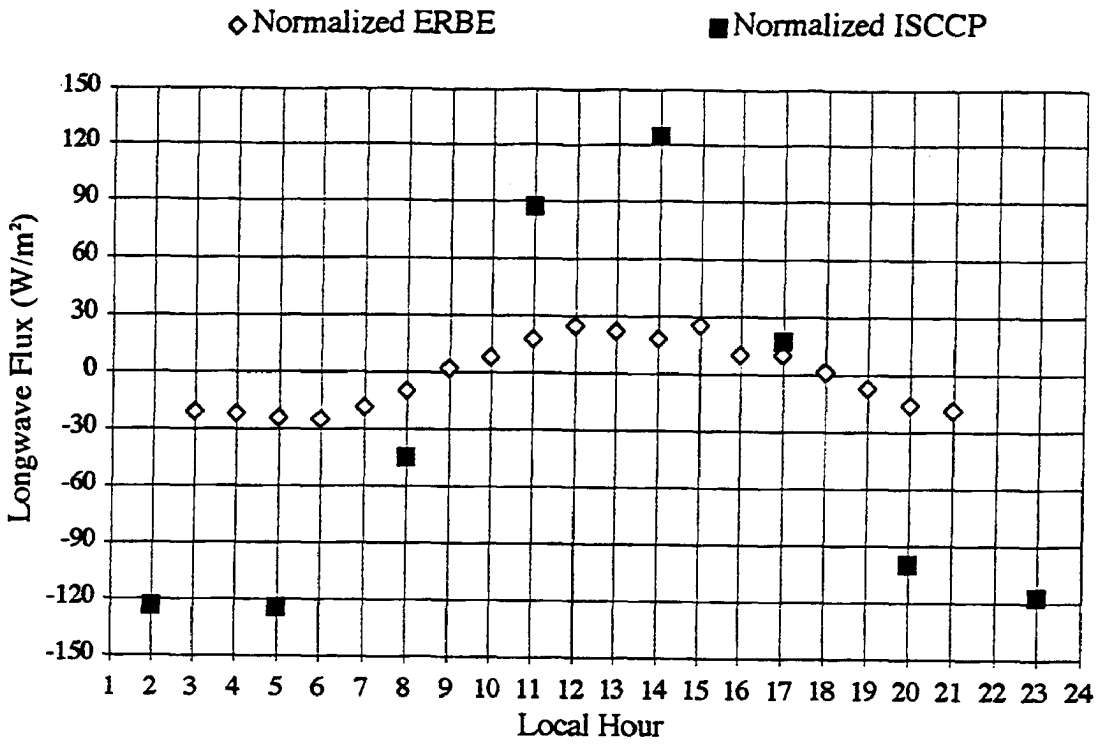

Figure 3.5. Amplitude of ISCCP flux curve adjusted to the amplitude of the ERBE flux curve.

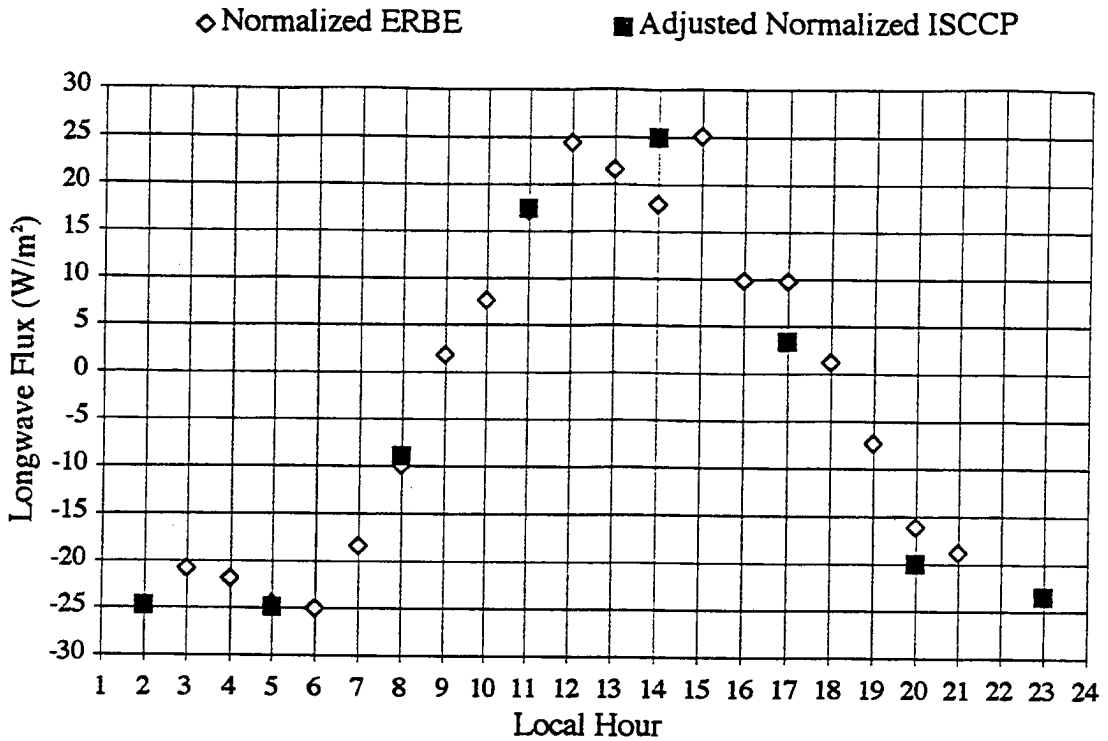

Figure 3.6. Return of flux curves to their relative positions prior to normalization.

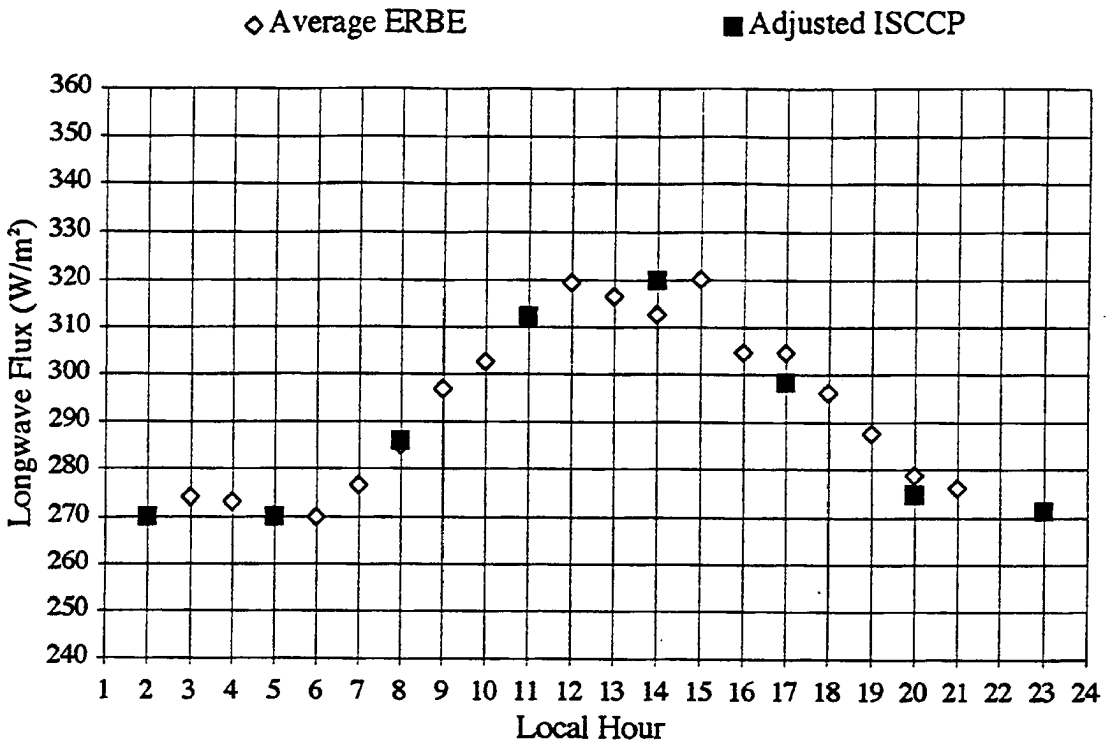

Figure 3.7. ERBE S-9 hourly data with missing ERBE hours interpolated with coincident adjusted ISCCP data.

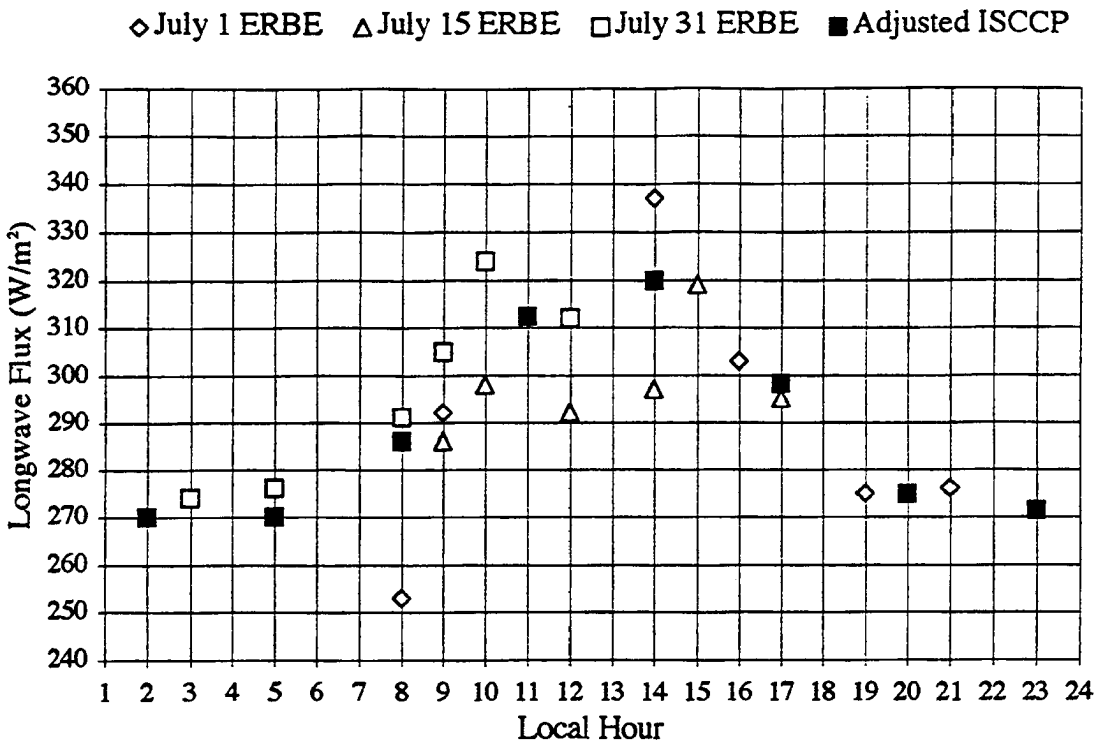

Figure 3.8. Difference in W/m^2 between ERBE S-4 monthly averaged clear sky OLR and ERBE/ISCCP interpolated monthly mean clear sky OLR computed from daily averages for July 1988.

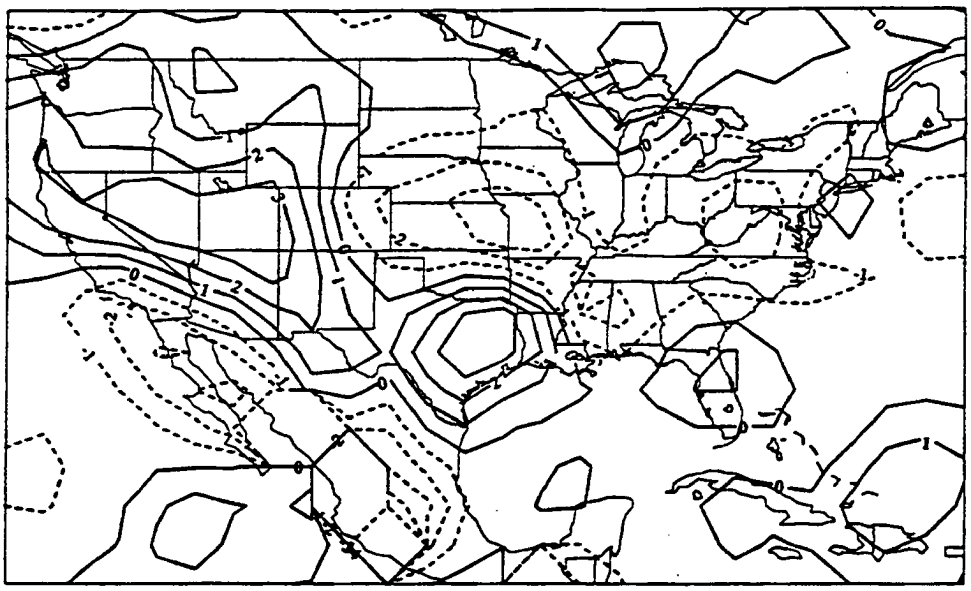

shows the difference between the ERBE/ISCCP monthly averaged clear sky OLR and the ERBE S-4 monthly averaged clear sky OLR.

3.2 CLEAR SKY OLR OVER OCEANS

Conditions over the oceans are much less variable in time and space than over land. Clear sky OLR over oceans generally does not exhibit a pronounced diurnal variation. Thus for this study, the ERBE averaging system was sufficient for producing daily values of clear sky OLR over oceans. Figure 3.9 depicts a flowchart showing the interpolation of missing data point over the oceans.

As in the ERBE averaging system (Satran, *et al.*, 1986), all hour boxes for a particular month were filled with existing data. Empty boxes at the beginning and end of a month were extrapolated backward and forward respectively from the first available data point closest to the beginning or end of the month. Missing hourly data throughout the month were filled using linear interpolation between existing data points. Daily averages were then calculated from the filled data boxes. Monthly averages were computed from the daily averages and were compared with the ERBE S-4 monthly averages. The comparison can be seen by referring once again to Figure 3.8 where differences over oceans were generally zero.

Figure 3.9. Flowchart depicting the method used to interpolate missing ERBE hourly data points over water using extrapolation and interpolation of existing hourly data.

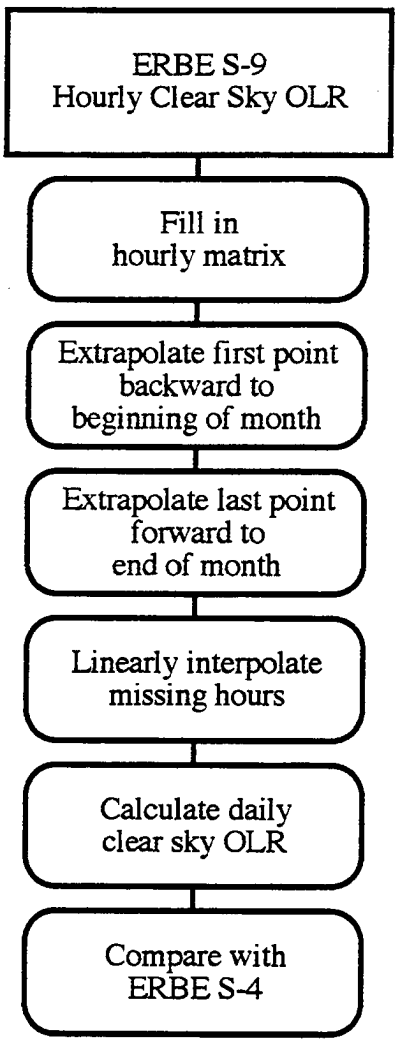

Chapter 4

OUTGOING LONGWAVE RADIATION SENSITIVITY

Selective atmospheric absorption and emission of longwave or infrared radiation in the spectral range of 4 μm to 50 μm is mainly due to water vapor, carbon dioxide, ozone, and some minor constituents (Coulson, 1975; Sellers, 1965). Relatively little energy is emitted in the atmospheric window region between 8 and 13 μm, whereas strong absorption and emission bands occur between 5 and 8 μm and beyond 20 μm for water vapor, and between 14 and 16 μm for carbon dioxide. The ground surface emits radiation as a graybody to approximately a blackbody in the infrared wavelengths. The longwave radiation which reaches the ground from the clear sky above is mainly due to emission by atmospheric gases, primarily water vapor. Thus, longwave radiation emitted to space from the ground and a clear atmosphere is composed mainly of that emitted by the atmosphere in wavelengths of strong absorption bands plus that which is emitted by the surface and transmitted outward in the regions of weak atmospheric absorption.

Fluctuations in the amount of longwave radiation passing unabsorbed to space from the ground are associated mainly with variations in the surface temperature and in the amount of water vapor in the clear sky atmosphere which itself is a function of temperature. The net outgoing longwave radiation from the surface is considerably reduced from what would be observed if the atmosphere did not contain absorbing gases such as water vapor. This reduction of outgoing longwave radiation by atmospheric constituents has the dubious distinction as the "greenhouse effect", and Bohren (1987) gave an insightful and entertaining discussion of this distinction.

There have been various studies conducted on the effects of water vapor on the longwave radiation balance of the atmosphere. Most of these have concentrated on tropical ocean areas in order to minimize problems associated with the variable nature of land surfaces. The third study in this research used the LOWTRAN7 radiative transfer model to help uncover some of the relationships among vertical water vapor distribution, vertical temperature profiles, and clear sky outgoing longwave radiation.

Manabe and Wetherald (1967) provided a thorough discussion of the relationships involved in the thermal equilibrium of the atmosphere. The absolute humidity in the atmosphere strongly depends on temperature. If the moisture content of the atmosphere depends upon atmospheric temperature, the effective height of the source of outgoing longwave radiation also depends upon atmospheric temperature. Given a vertical distribution of relative humidity, the warmer the atmospheric temperature, the higher the effective source of outgoing radiation. Also, the dependence of the outgoing longwave radiation is less than that to be expected from the fourth-power law of Stefan-Boltzmann. Therefore, the equilibrium temperature of the atmosphere with a fixed relative humidity depends more upon atmospheric absorbers such as water vapor than does an atmosphere with a fixed absolute humidity in order to satisfy radiative convective equilibrium.

4.1 WATER VAPOR FORCING EFFECT

One method for exploring the sensitivity relationship between water vapor and clear sky OLR has been defined as "water vapor forcing" by Randel, *et al.* (1993). Simply stated,

$$WV_{forcing} = (WV_{min} - WV_{obs}) \times S$$

where WV_{min} was the annual minimum observed value of water vapor at a particular grid location, WV_{obs} was the average observed value of water vapor for a particular month, and S was a sensitivity relationship between water vapor and clear sky outgoing longwave radiation. $WV_{forcing}$ has units of W/m^2. The fact that column-integrated atmospheric water

vapor never equals zero was the reason for using the annual minimum observed value in the calculations. The sensitivity parameter, S, was determined from application of a least absolute deviations (LAD) regression analysis to daily values of water vapor versus clear sky OLR for one month. Statistical significance of the sensitivity parameter was evaluated using a multivariate randomized block permutation test (Peterson, 1991; Mielke, 1984). This test assigned a P-value, or probability that the sensitivity parameter, S, was the result of a random arrangement of water vapor/OLR values, at each grid location.

This method has been applied with success over tropical and subtropical oceans where daily values of clear sky OLR are readily accessible, surface temperatures vary slowly in time and space, and thermal emissivity values are approximately one. Sensitivity slopes derived from the regression analysis generally are negative, implying an inverse relationship between water vapor and clear sky OLR. Using the definition above, fields of $WV_{forcing}$ were generally positive and detailed the decrease in top-of-the-atmosphere clear sky OLR with an increase in water vapor above the observed background minimum.

Originally, this study attempted to apply the method of Randel, *et al.* (1993) over mid-latitude land surfaces. This attempt resulted in many difficulties. Because of the highly variable nature of the land surface—due to large diurnal temperature changes, the influence of synoptic weather patterns, and uncertainties in the thermal emissivities—sensitivity parameters were quite variable and exhibited both negative and positive values. The uncertainties in thermal emissivities of natural surfaces alone are due to differences in soil structure, soil composition, organic matter, moisture content, and differences in vegetation cover characteristics (Van de Griend and Owe, 1993).

Figure 4.1 shows a scatter diagram of precipitable water versus clear sky OLR for a 2°x2° grid point over the United States for July 1988. The LAD regression analysis indicated a negative sensitivity slope; however, the degree of scatter was quite large. Fields of $WV_{forcing}$ over land, as Figure 4.2 shows, exhibited both positive and negative values indicating that variables other than water vapor—most likely temperature—were

Figure 4.1. Scatter diagram of daily values of precipitable water (mm) versus ERBE/ISCCP interpolated clear sky OLR (W/m^2) for a 2°x2° grid centered at 33°N latitude and 101°W longitude over west-central Texas for July 1988. The best fit line from the least absolute deviations regression analysis is also shown.

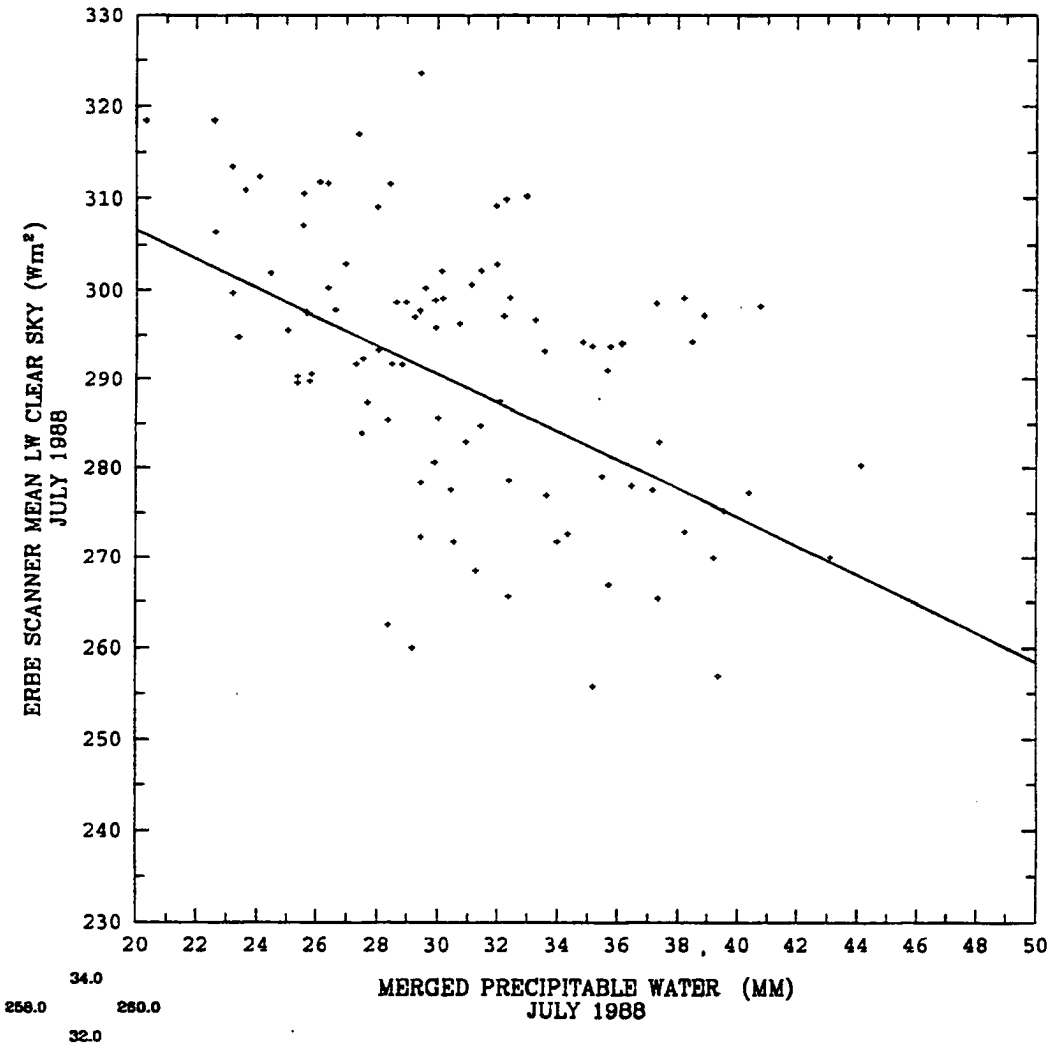

Figure 4.2. Map of $WV_{forcing}$ in W/m^2 for July 1988. Positive values of $WV_{forcing}$ are solid, and negative values of $WV_{forcing}$ are dashed.

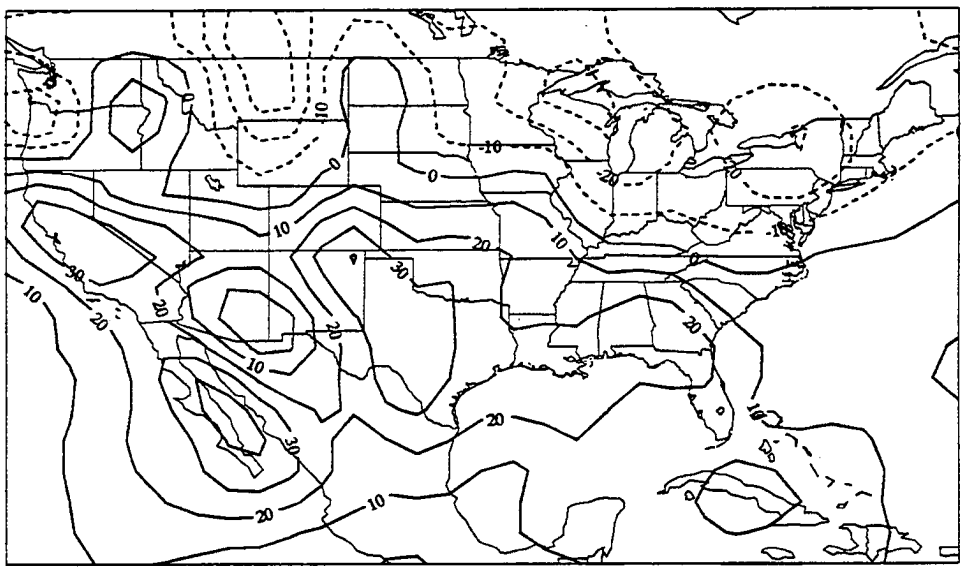

influencing clear sky OLR. Simply put, the water vapor/OLR sensitivity did not exhibit a linear relationship over land.

One interesting influence that may cause values of $WV_{forcing}$ to be negative is the effects of a moistening inversion layer. This possibility was explored using the LOWTRAN7 radiative transfer model, which will be discussed more fully in Sections 4.3 and 4.4. This test simulated the effects on clear sky OLR when a temperature inversion was present at 850 hPa, and precipitable water contents were increasing in the 850 to 700 hPa layer. Table 4.1 depicts the values used for temperature and precipitable water during each of the four tests. Figure 4.3 indicates that for an increase in precipitable water between 850 and 700 hPa, with an inversion at 850 hPa, there is a corresponding increase in clear sky OLR. In terms of water vapor forcing theory, Figure 4.3 is analogous to negative values of $WV_{forcing}$ in which an increase in clear sky OLR occurs for an increase in water vapor. This is counter-intuitive to our understanding of water vapor as a trapping greenhouse gas.

The inversion, together with the increasing moisture above the surface, allows for emission of infrared radiation at a higher level in the atmosphere where the atmospheric temperature is warmer than the surface. The increasing moisture in the 850 to 700 hPa layer effectively shields more of the surface emission which occurs at a lower temperature than the inversion level. The increasing water vapor limits more of the surface infrared emission by changing the optical depth of the atmosphere. Thus, emission occurs closer and closer to the higher temperature of the inversion level leading to increased clear sky OLR. (Kidder and Vonder Haar, 1992)

Table 4.1: Calculated values of clear sky OLR (W/m^2) for four LOWTRAN model runs simulating a moistening inversion layer. The inversion is centered at 850 hPa, and the increasing precipitable water is in the 850 to 700 hPa layer. Values of precipitable water are in mm.

p (hPa)	T (K)	PW (test #1)	PW (test #2)	PW (test #3)	PW (test #4)
1000	285	8.1	8.1	8.1	8.1
850	290	6.0	6.8	7.5	8.0
700	277	3.5	3.5	3.5	3.5
600	270	1.3	1.3	1.3	1.3
500	262	0.7	0.7	0.7	0.7
400	255	0.6	0.6	0.6	0.6
Calculated OLR (W/m^2):		253.84	253.90	253.98	254.01

Figure 4.3. LOWTRAN7 results for calculated values of clear sky OLR (W/m^2) for a moistening inversion layer. The inversion is centered at 850 hPa and the increasing precipitable water (mm) occurs in a layer from 850 to 700 hPa.

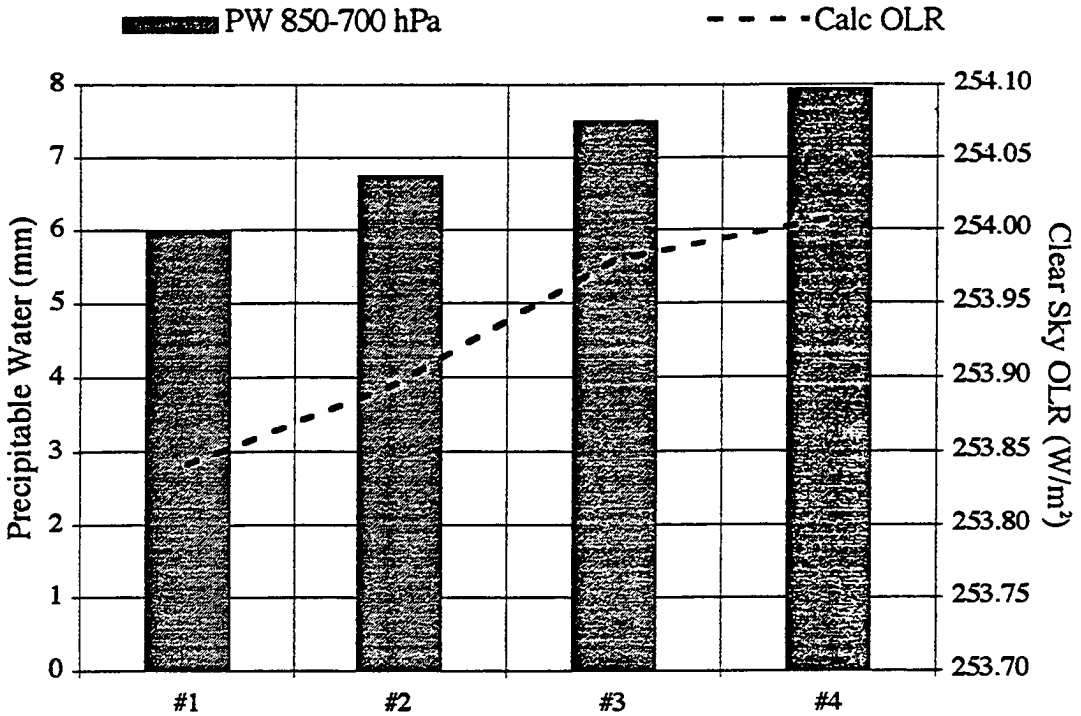

4.2 CLEAR SKY ATMOSPHERIC GREENHOUSE EFFECT

The earth-atmosphere system absorbs solar radiation and maintains global energy balance by radiating energy back to space as infrared or longwave radiation. The atmosphere both absorbs and emits longwave radiation, but since the atmosphere is colder than the surface it absorbs more energy than it emits upward to space. The difference between what is emitted at the surface and what is emitted to space is the energy trapped by the atmosphere. Thus, the clear sky atmospheric greenhouse effect is defined as the infrared radiation energy trapped by atmospheric gases, the major gas being water vapor (Raval and Ramanathan, 1989).

Analysis of the clear sky greenhouse effect has shown that it is determined mainly by the distributions of temperature and atmospheric water vapor. Raval and Ramanathan (1989) used ERBE radiation budget data to show the existence of a strong positive correlation between the clear sky greenhouse effect over the oceans and the sea surface temperature. Stephens and Greenwald (1991) performed a similar analysis and showed that the observed relationships were consistent with a simple gray body radiative model. Their numerical experiments further showed that the clear sky greenhouse effect was not only dependent on the total column moisture content, but also on the temperature and humidity profiles.

The clear sky greenhouse effect (in W/m^2) may be defined as the difference between the longwave emission from the surface (E) and the emission from the top of a clear atmosphere (F_{clear}):

$$G_A = E - F_{clear}$$

where,

$$E = \varepsilon_s \sigma T_s^4$$

where ε_s is the surface emissivity and T_s is the surface temperature. F_{clear} is determined from ERBE measurements and can also be calculated using:

$$F_{clear} = \varepsilon_A \sigma T_A^4 + (1-\varepsilon_A)\sigma T_s^4$$

where ε_A is the mean atmospheric emissivity and T_A is the mean atmospheric temperature. The first term represents the atmospheric emission and the second term represents the flux emitted upward from the surface to space which is partially absorbed by the atmosphere.

In order to remove the strong temperature dependence, it is desirable to use a normalized clear sky greenhouse effect as defined by Stephens and Greenwald (1991):

$$G = E/F_{clear}.$$

Therefore, G becomes:

$$G = (\varepsilon_s \sigma T_s^4)/[\varepsilon_A \sigma T_A^4 + (1-\varepsilon_A)\sigma T_s^4].$$

This equation illustrates the effects of temperature, emissivity, and precipitable water (through ε_A) on the clear sky greenhouse effect. Increases in precipitable water, and thus ε_A lead to increases in G. Meanwhile, increases in T_A lead to a reduction of the temperature contrast between the atmosphere and the surface, and thus a lower G.

Bony and Duvel (1993) explored the seasonal variations of precipitable water and greenhouse effect over ocean and land regions. For Northern Hemisphere land regions, the seasonal variations of lapse rate and relative humidity acted to reduce the large seasonal amplitude of the precipitable water. The amplitude of the precipitable water itself was related to the large seasonal variation of the surface temperature. This reduction occurred because a smaller winter lapse rate increased the water storage capacity in altitude and thus the precipitable water in altitude. Relative humidity variations also tended to increase the precipitable water in winter. The seasonal amplitude of the clear-sky greenhouse effect was enhanced by lapse rate variations and reduced by relative humidity variations.

Galin, *et al.*, (1991) investigated the dependence of outgoing and incoming clear sky IR radiation fluxes on temperature and humidity as calculated from various climatic models and from shipboard radiometer soundings. The outgoing flux was found to approach the flux emitted at the earth's surface with decreasing moisture content of the atmosphere. Furthermore, both fluxes showed a strong temperature dependence with

increasing IR flux for increasing surface temperature. At temperatures above 280 K, the temperature dependence was strongest with the moisture dependence nearly disappearing. This relationship may be related to the "super greenhouse effect" described by Ramanathan and Collins (1991) in which the magnitude of the clear sky greenhouse effect increased rapidly as sea surface temperatures reached their maximum values.

Peterson (1991) studied changes in clear sky greenhouse effect over oceans related to changes in three-layer precipitable water using a two-stream IR radiative transfer model. The three layers used in this study were surface to 800 hPa, 800 to 560 hPa, and 560 to 310 hPa. His results indicated, on average over the oceans, positive changes in water vapor associated with a 1 K increase in sea surface temperature at each of the three levels increased the greenhouse effect (a decrease in clear sky OLR). The increase was greatest when all three layers of water vapor were used. More importantly, of the individual layers, the layer highest in the atmosphere had the greatest radiative effect and the lowest layer had the smallest radiative effect.

As with water vapor forcing, the simple method of calculating the clear sky greenhouse effect over mid-latitude land surfaces becomes a challenge due to the variability in thermal emissivity, the diurnal cycle, and synoptic influences. Thus, a radiative transfer model was utilized in this study to help uncover the relationships among, temperature, water vapor, and clear sky OLR.

4.3 LOWTRAN7 SIMULATIONS

The LOWTRAN7 model and computer code is a band model which calculates atmospheric transmittance and thermal radiance for a given atmospheric path at low spectral resolution. Representative atmospheric models as well as an atmospheric data base consisting of separate molecular profiles for thirteen minor and trace gases are provided by the model. Six reference atmospheres, each defining temperature, pressure, density, and mixing ratios for atmospheric gases such as water vapor, all as a function of altitude, allow

for a range of climatological choices (Kneizys, *et al.*, 1988). User defined atmospheres can be specified as well.

In this study, the LOWTRAN7 model was run for three simulations to test the relationships among atmospheric water vapor, surface and atmospheric temperatures, and clear sky OLR. Three different simulations of twenty cases each were performed to calculate top-of-the-atmosphere clear sky OLR: 1) using observed values of temperature and precipitable water to compare against observed clear sky OLR, 2) using observed ECMWF temperatures while holding precipitable water constant, and 3) using observed values of precipitable water while holding temperatures constant. The twenty cases represented various land locations over the United States, Canada, and Mexico.

Observations of three-layer precipitable water from the merged dataset and temperature from ECMWF analyses for July 15, 1988 were substituted into the model at the surface, 700 hPa, and 500 hPa. Daily 0000 GMT temperature data were obtained from the National Center for Atmospheric Research (NCAR) archive of operational analyses of the European Centre for Medium Range Weather Forecasts (ECMWF). Otherwise, remaining atmospheric parameters, such as trace gas and aerosol distributions, were assigned values using the mid-latitude summer model contained within LOWTRAN7. Published studies of thermal emissivity were consulted (Van de Griend and Owe, 1993; Sellers, 1965), and a surface thermal emissivity of 0.95 was used in the simulations. Calculations were performed through an atmospheric path from the surface to the top-of-the-atmosphere at 10° zenith angle intervals from nadir to limb. Computed radiances for each zenith angle interval were integrated to calculate the total top-of-the-atmosphere longwave flux.

4.4 LOWTRAN7 RESULTS

Results from LOWTRAN7 comparing calculated to observed values of clear sky OLR with both temperature and precipitable water observations are presented in Figures

4.4 through 4.6, and Figures 4.8 through 4.11. Linear regression using a least squares fit was performed for each figure, and the correlation coefficient was calculated and is indicated on each of the graphs. Table 4.2 details the observed values of temperature and precipitable water used in this first simulation.

Figures 4.4 through 4.6 show temperature versus clear sky OLR determined from observations and calculated by LOWTRAN7. The temperatures in Figures 4.4, 4.5, and 4.6 represent the surface, 700 hPa, and 500 hPa temperatures respectively, and were determined from ECMWF analyses of July 15, 1988. All three graphs exhibit a positive correlation between the observed temperature and observed and calculated values of clear sky OLR. The calculated OLR results show the strongest correlation with the temperature as the LOWTRAN7 model eliminates some of the variables found in the observations.

At relatively cooler temperatures, the graphs of observed and calculated clear sky OLR generally coincide. The OLR curves diverge as temperatures become warmer but still maintain a positive correlation with the temperatures. The divergence of the graphs mainly results from simplifying the atmosphere into three layers to accommodate the observed data. Variable topography affecting the surface station pressure and elevation may also introduce model differences in the surface to 700 hPa layer. However, both OLR curves seem to indicate a general increase in clear sky OLR with increasing temperature, as would be expected given the Stefan-Boltzmann relationship.

A supplementary LOWTRAN7 simulation was run to help explain the divergence of the observed and calculated clear sky OLR curves. Values of precipitable water were interpolated from the layered data to increase the number of atmospheric layers from three to six. These layers included surface to 850 hPa, 850 to 700 hPa, 700 to 600 hPa, 600 to 500 hPa, 500 to 400 hPa, and 400 to 300 hPa. Temperature data was again taken from ECMWF analyses corresponding to the precipitable water levels. Figure 4.7 shows the results of this simulation.

Figure 4.4. LOWTRAN7 results for observed surface temperatures versus observed and calculated clear sky OLR for July 15, 1988 for selected sites over land. Linear regression using a least squares fit has been performed on each set of clear sky OLR data, and correlation coefficients (r-values) are indicated.

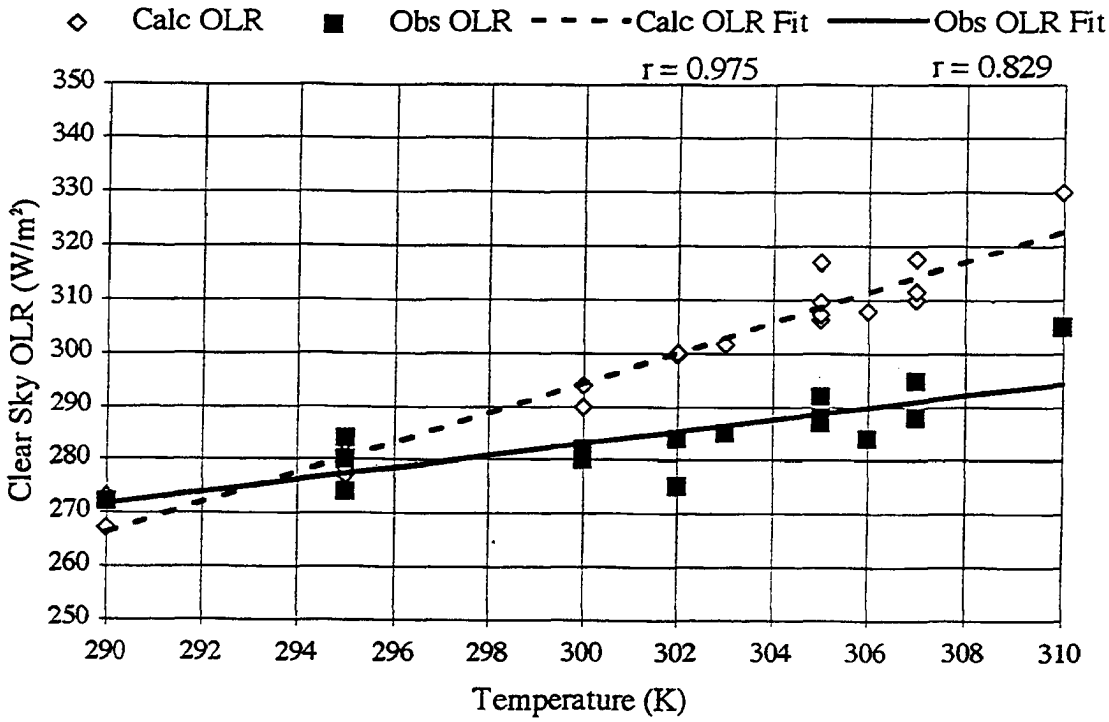

Figure 4.5. LOWTRAN7 results for observed 700 hPa temperatures versus observed and calculated clear sky OLR for July 15, 1988 for selected sites over land. Linear regression using a least squares fit has been performed on each set of clear sky OLR data, and correlation coefficients (r-values) are indicated.

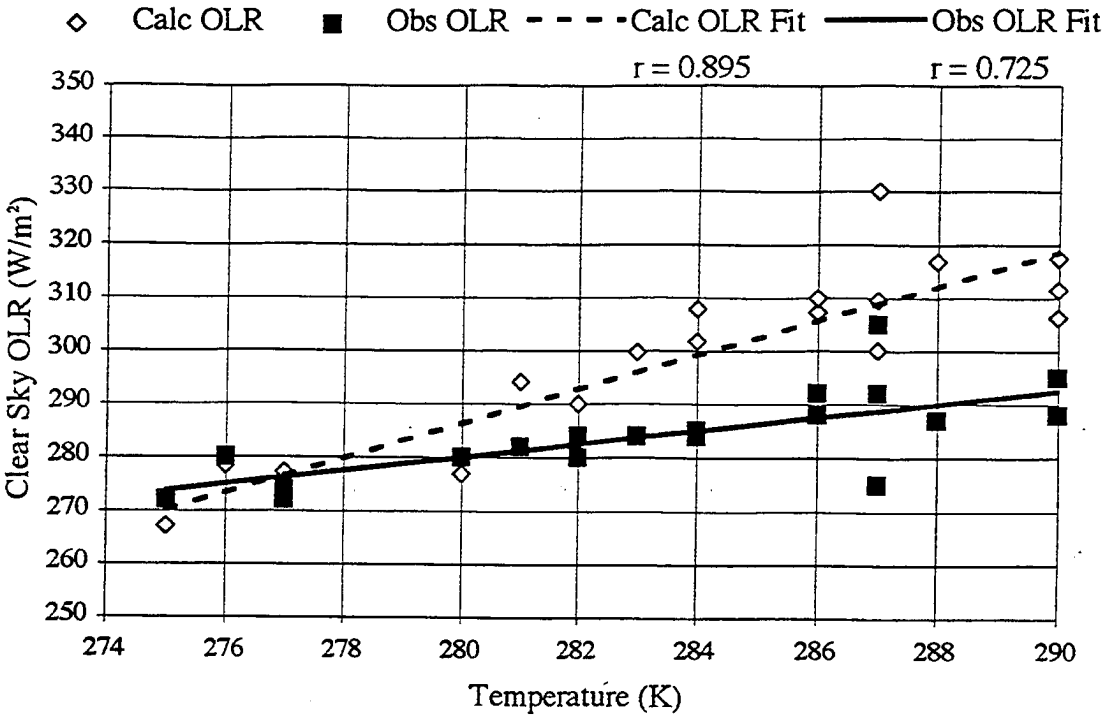

Figure 4.6. LOWTRAN7 results for observed 500 hPa temperatures versus observed and calculated clear sky OLR for July 15, 1988 for selected sites over land. Linear regression using a least squares fit has been performed on each set of clear sky OLR data, and correlation coefficients (r-values) are indicated.

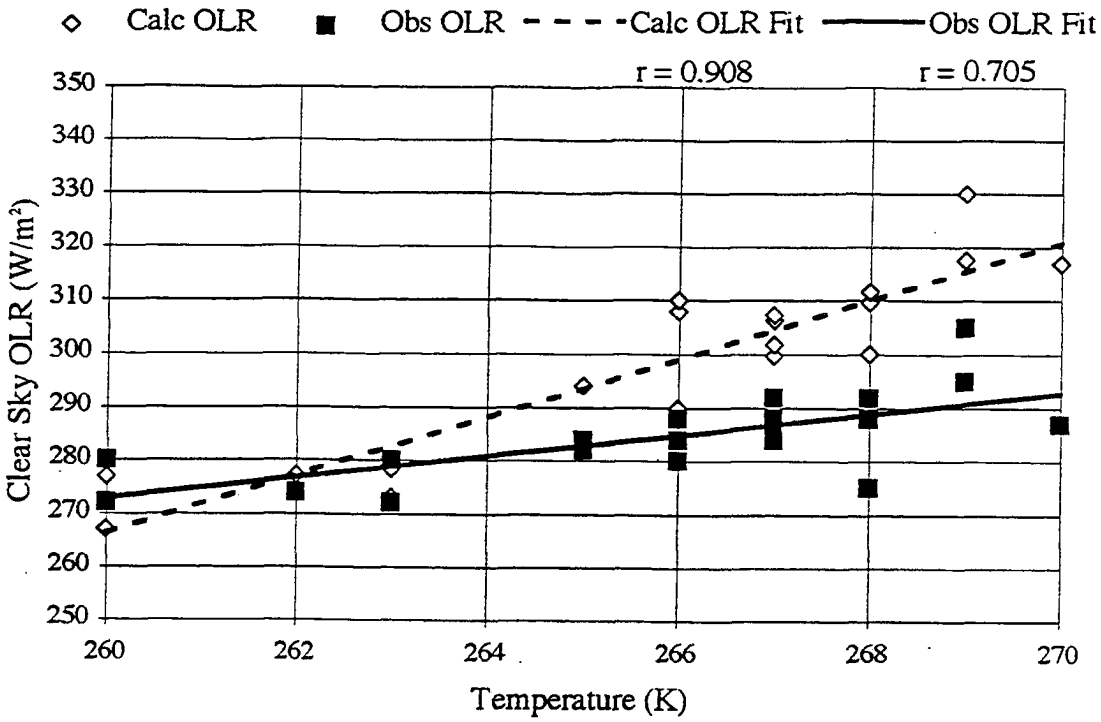

Table 4.2: Calculated and observed values of clear sky OLR (W/m^2) for twenty selected sites for July 15, 1988. The calculated values were computed from observed values of precipitable water (mm) and temperature (K) for a three-layer atmosphere of surface to 700 hPa, 700 to 500 hPa, and 500 to 300 hPa.

	PW1 Sfc-700	PW2 700-500	PW3 500-300	Temp1 Sfc	Temp2 700 hPa	Temp3 500 hPa	OLR Calc	OLR Obs
CN	15.0	4.0	1.2	290	275	260	267.0	272
ME	18.0	4.0	1.0	290	277	263	273.0	272
ID	11.0	6.0	1.5	295	280	260	276.9	280
MN	21.0	7.0	1.7	295	277	262	277.2	274
OR	18.0	5.0	2.0	295	276	263	278.4	280
ND	21.0	7.0	2.0	295	282	265	283.0	284
FL	39.0	10.0	3.0	300	282	266	289.9	280
PA	25.0	7.0	1.5	300	281	265	294.1	282
NC	33.0	8.0	2.0	302	283	267	299.6	284
MX	12.0	10.0	3.0	302	287	268	300.1	275
AL	36.0	8.5	2.0	303	284	267	301.7	285
CO	12.0	8.0	3.0	305	290	267	306.2	288
AR	33.0	8.0	2.0	305	286	267	307.2	292
IN	27.0	6.0	2.0	306	284	266	307.8	284
TX	30.0	8.0	2.0	305	287	268	309.4	292
NE	27.0	8.0	2.0	307	286	266	309.9	288
NM	12.0	10.0	3.0	307	290	268	311.5	288
BJ	24.0	5.0	1.5	305	288	270	316.8	287
AZ	12.0	8.0	2.0	307	290	269	317.4	295
CA	15.0	4.0	1.0	310	287	269	329.9	305

Figure 4.7. LOWTRAN7 results of calculated versus observed values of clear sky OLR (W/m^2) using a six layer atmosphere with both observed and interpolated precipitable water data.

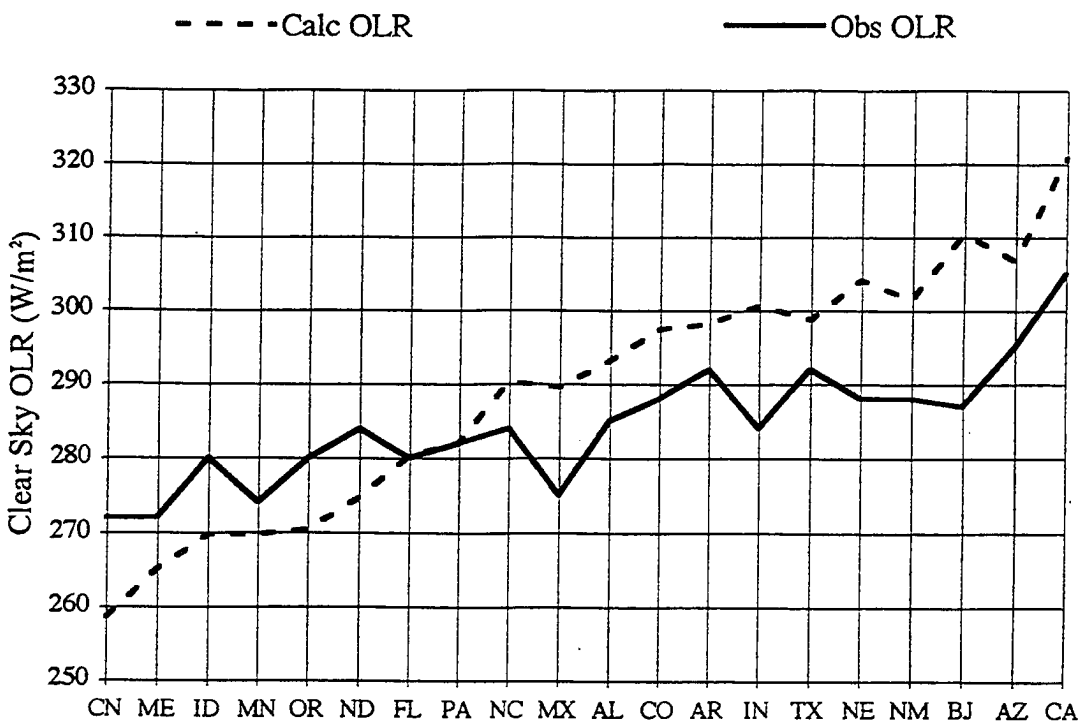

The curves still exhibit some divergence, but the magnitude of the divergence has decreased. Further, the divergence is found at both the lower and upper ranges in the clear sky OLR values with the crossover point closer to the center of the range. The calculated clear sky OLR curve shows a larger slope than the observed curve, but this slope is slightly smaller than the slope in the original simulation.

These results would seem to indicate that the simplification of the atmosphere into three layers was the cause of the divergence of the curves in the original simulation. With more detailed layered precipitable water data—achieved only through additional interpolation—improvements in the calculations of clear sky OLR using LOWTRAN7 could be expected. However, for the purpose of this investigation, it is desired to use the least amount of interpolation and remain with observations. In doing so, some accuracy in calculated clear sky OLRs will be lost, and LOWTRAN7 values of clear sky OLR at relatively warmer temperatures will be higher than observed values of clear sky OLR. The average temperature profile of the three-layer atmosphere is warmer than that of the six-layer atmosphere, and thus calculated infrared emissions will be higher in the three-layer atmosphere. Nevertheless, the original simulation with its three-layer atmosphere exhibits the expected increasing trend in the calculated clear sky OLRs with increasing temperature; thus, the three-layer atmosphere will continue to be used for the rest of this investigation.

Figure 4.8 shows the total column-integrated precipitable water versus the observed and calculated clear sky OLR. Figures 4.9, 4.10, and 4.11 break the integrated precipitable water into their respective layers of surface to 700 hPa, 700 to 500 hPa, and 500 to 300 hPa. Initially, a negative correlation between precipitable water and clear sky OLR was expected to be found, based upon the results of greenhouse effect experiments discussed earlier. However, the data in Figure 4.8 showed an insignificant positive correlation between total precipitable water and clear sky OLR. The individual precipitable water layers showed this same small positive correlation with clear sky OLR. It would appear that the water vapor/OLR signal was masked by the temperature influence on the precipitable water.

Figure 4.8. LOWTRAN7 results for observed total column-integrated precipitable water versus observed and calculated clear sky OLR for July 15, 1988 for selected sites over land. Linear regression using a least squares fit has been performed on each set of clear sky OLR data, and correlation coefficients (r-values) are indicated.

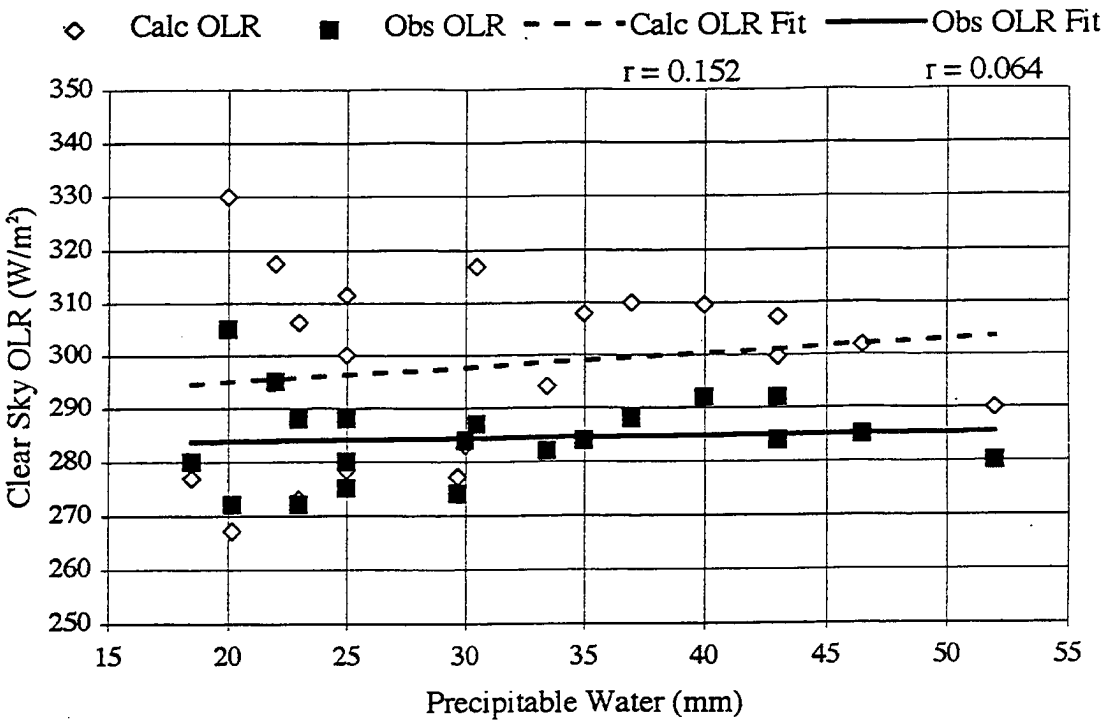

Figure 4.9. LOWTRAN7 results for observed precipitable water in the surface to 700 hPa layer versus observed and calculated clear sky OLR for July 15, 1988 for selected sites over land. Linear regression using a least squares fit has been performed on each set of clear sky OLR data, and correlation coefficients (r-values) are indicated.

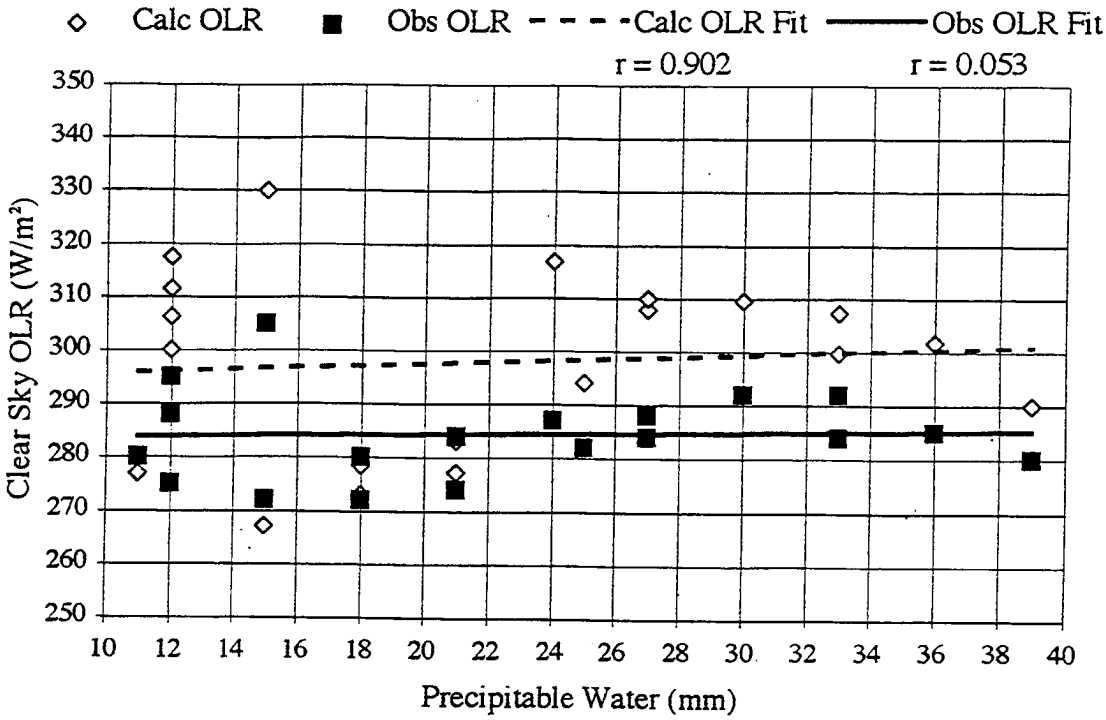

Figure 4.10. LOWTRAN7 results for observed precipitable water in the 700 to 500 hPa layer versus observed and calculated clear sky OLR for July 15, 1988 for selected sites over land. Linear regression using a least squares fit has been performed on each set of clear sky OLR data, and correlation coefficients (r-values) are indicated.

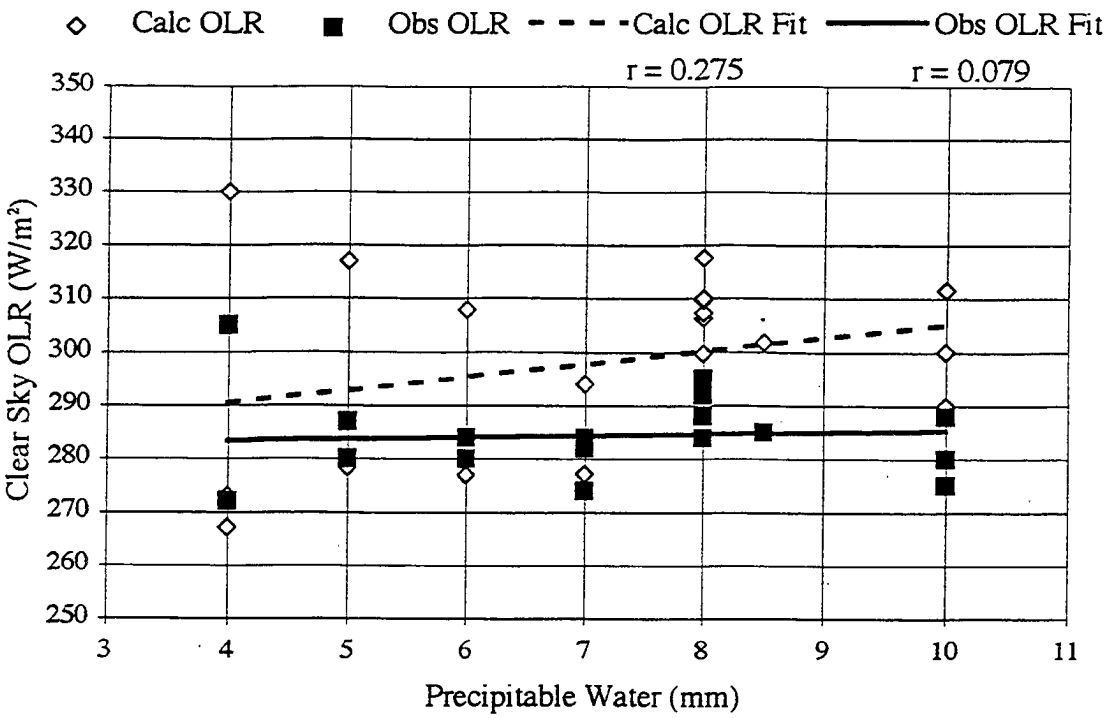

Figure 4.11. LOWTRAN7 results for observed precipitable water in the 500 to 300 hPa layer versus observed and calculated clear sky OLR for July 15, 1988 for selected sites over land. Linear regression using a least squares fit has been performed on each set of clear sky OLR data, and correlation coefficients (r-values) are indicated.

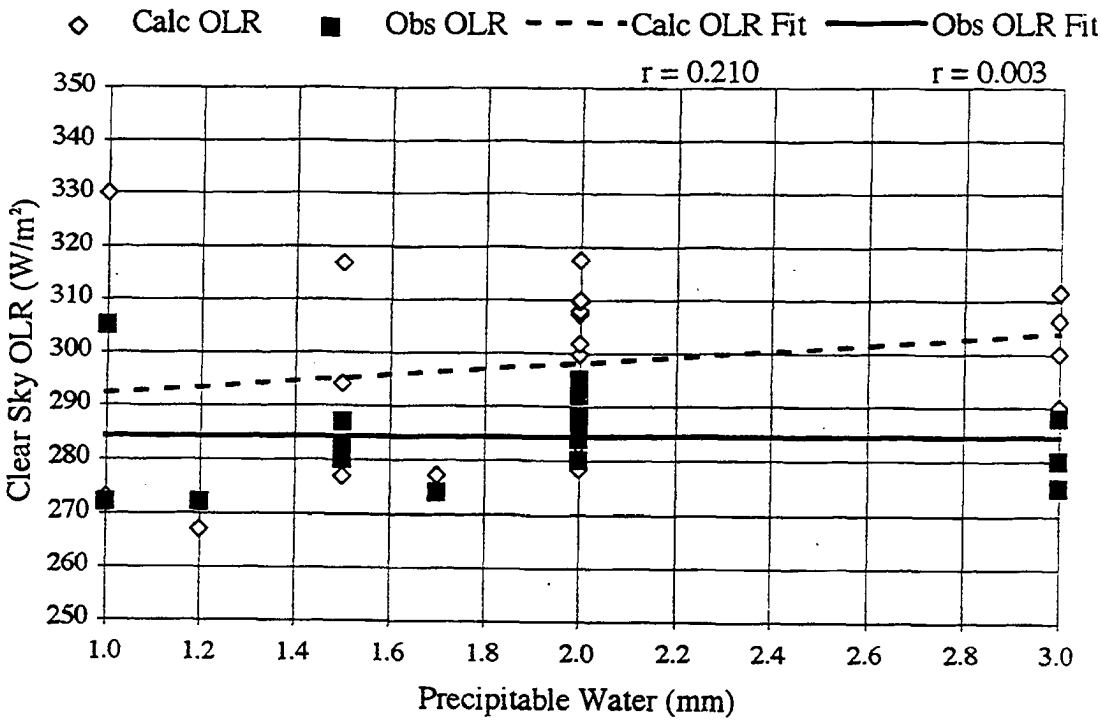

Thus, over mid-latitude land surfaces, the dominant influence on clear sky OLR is not the precipitable water, but the temperature.

This hypothesis was further supported in the second simulation where precipitable water amounts were held constant while the temperatures were varied. This simulation sought to remove any variation of precipitable water due to non-thermodynamic effects, such as horizontal advection or convergence. The constant precipitable water amounts represented an approximate average of the observed precipitable water from the first simulation. Figures 4.12 through 4.14 show calculated values of clear sky OLR for varying surface, 700 hPa, and 500 hPa temperatures taken from the July 15, 1988 ECMWF observations. Again, linear regression using a least squares fit was performed for each figure, and the correlation coefficient was calculated and is indicated on each of the graphs. Table 4.3 details the observed values of temperature and the constant layered precipitable water amounts used in this simulation.

Based upon this simulation, temperature appeared to be the dominant influence on clear sky OLR. Figures 4.12 through 4.14 show a very strong positive correlation between temperature and top-of-the-atmosphere clear sky OLR. The highest positive correlation ($r=0.986$) is found at the surface where the warmest temperatures, and thus the greatest infrared emission, occur. The positive correlation decreases with altitude, but is still greater than 0.92 at 500 hPa. Overall, the positive correlations in the three figures support the expected Stefan-Boltzmann-type relationship between temperature and clear sky OLR.

Finally, the third simulation examined the relationship of water vapor to clear sky OLR in the absence of temperature variations. It was hoped that this simulation would reveal the true nature of water vapor as an infrared-trapping greenhouse gas. In particular, this simulation was run to uncover the negative correlation expected between the water vapor content of the atmosphere and the clear sky OLR. The objective was achieved, especially in the upper troposphere.

The simulation held the temperature profile constant while varying the precipitable water amounts taken from the merged data set. This simulation hoped to remove most of the dependence of the precipitable water on the temperature profile as dictated by the Clausius-Clapeyron equation. The constant temperatures represented an approximate average of the observed temperatures from the first simulation. Figure 4.15 presents the calculated clear sky OLR versus total column-integrated precipitable water values taken from the merged data set. The least squares fit line and correlation coefficient are presented in this figure as well. The graph does exhibit a small degree of negative correlation between total precipitable water and clear sky OLR, but the relationship is not strong. Table 4.4 details the observed layered precipitable water amounts and the constant temperatures used for this simulation.

The graphs of Figures 4.16, 4.17, and 4.18 split the precipitable water into its layered amounts—surface to 700 hPa, 700 to 500 hPa, and 500 to 300 hPa. The precipitable water layers taken individually better reveal the sensitivity relationship between clear sky OLR and water vapor. The least squares fit lines and correlation coefficients are also shown in these figures.

The surface to 700 hPa layer presented in Figure 4.16 shows the weakest negative correlation; for example, widely varying precipitable water amounts occur for a nearly constant clear sky OLR value of approximately 295 W/m^2. Perhaps the distribution of water vapor in this layer is determined by the thermodynamic effects of a Clausius-Clapeyron relationship between temperature and water vapor, as well as the dynamic effects of horizontal advection and convergence of water vapor by the winds. Water vapor transport in the middle latitudes during summer exceeds that during winter and this transport can significantly enhance the precipitable water in these regions thus altering the thermodynamic relationship between temperature and precipitable water (Stephens, *et al.*, 1993). Also, mid-latitude land surface temperatures can be highly variable on a diurnal scale.

Figure 4.12. LOWTRAN7 results for observed surface temperatures versus calculated clear sky OLR with precipitable water held constant for July 15, 1988 for selected sites over land. Linear regression using a least squares fit has been performed on the clear sky OLR data, and the correlation coefficient (r-value) is indicated.

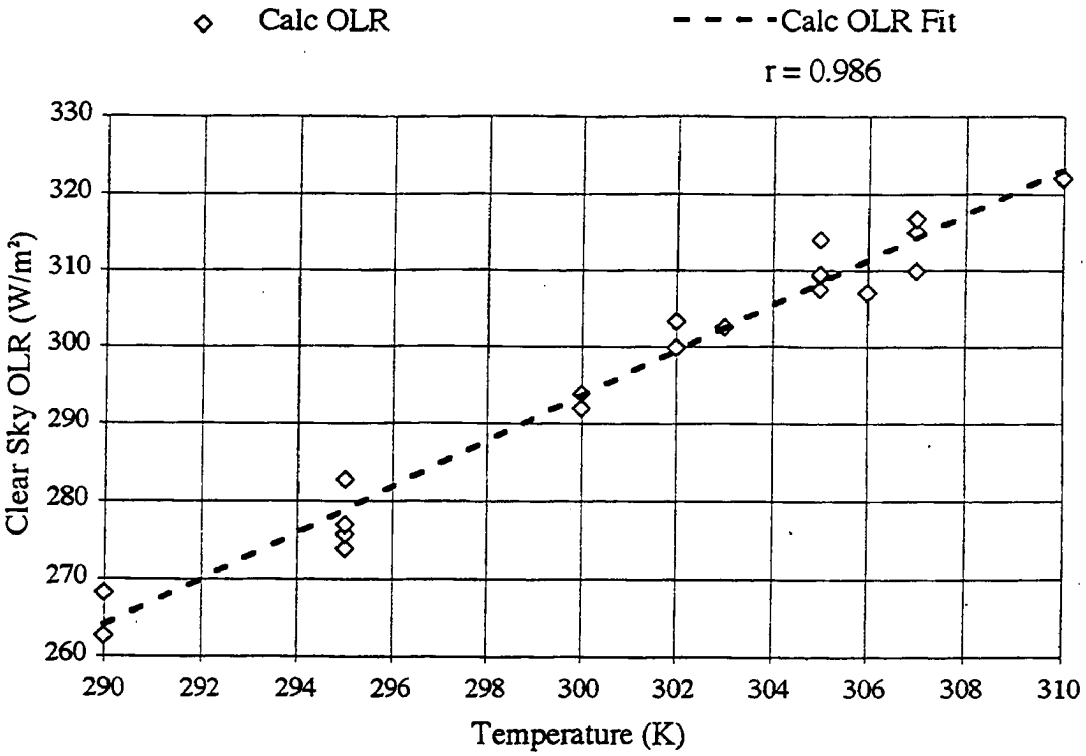

Figure 4.13. LOWTRAN7 results for observed 700 hPa temperatures versus calculated clear sky OLR with precipitable water held constant for July 15, 1988 for selected sites over land. Linear regression using a least squares fit has been performed on the clear sky OLR data, and the correlation coefficient (r-value) is indicated.

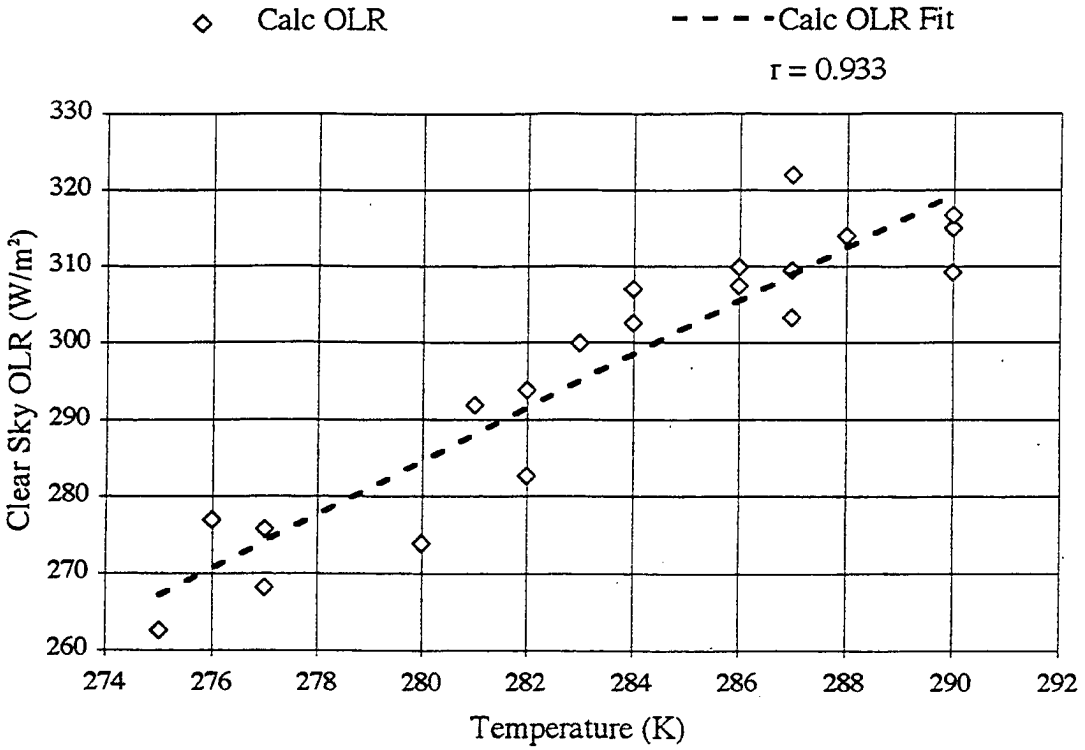

Figure 4.14. LOWTRAN7 results for observed 500 hPa temperatures versus calculated clear sky OLR with precipitable water held constant for July 15, 1988 for selected sites over land. Linear regression using a least squares fit has been performed on the clear sky OLR data, and the correlation coefficient (r-value) is indicated.

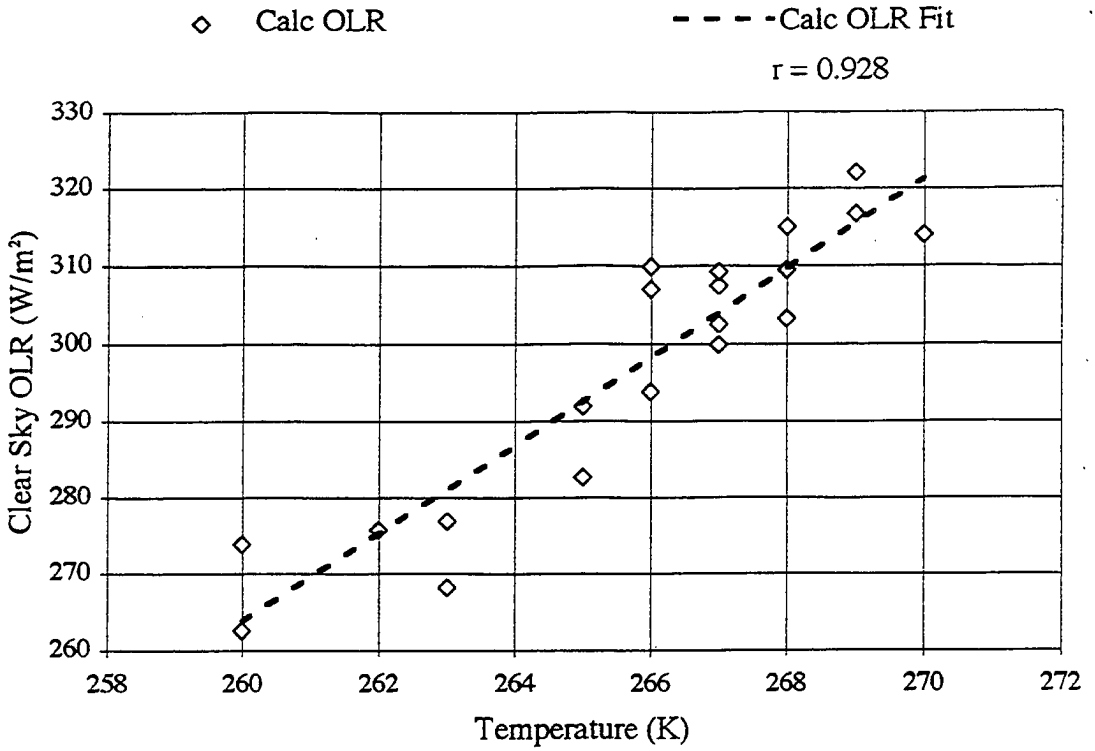

Table 4.3: Calculated values of clear sky OLR (W/m^2) for twenty LOWTRAN model runs. The calculated values were computed from constant values of precipitable water (mm) and observed temperatures (K) for a three-layer atmosphere of surface to 700 hPa, 700 to 500 hPa, and 500 to 300 hPa.

Test #	PW1 Sfc-700	PW2 700-500	PW3 500-300	Temp1 Sfc	Temp2 700 hPa	Temp3 500 hPa	OLR Calc
1	25.0	8.0	2.0	290	275	260	262.6
2	25.0	8.0	2.0	290	277	263	268.1
3	25.0	8.0	2.0	295	280	260	273.8
4	25.0	8.0	2.0	295	277	262	275.7
5	25.0	8.0	2.0	295	276	263	276.9
6	25.0	8.0	2.0	295	282	265	282.6
7	25.0	8.0	2.0	300	281	265	291.8
8	25.0	8.0	2.0	300	282	266	293.8
9	25.0	8.0	2.0	302	283	267	299.8
10	25.0	8.0	2.0	303	284	267	302.5
11	25.0	8.0	2.0	302	287	268	303.2
12	25.0	8.0	2.0	306	284	266	307.0
13	25.0	8.0	2.0	305	286	267	307.4
14	25.0	8.0	2.0	305	290	267	309.1
15	25.0	8.0	2.0	305	287	268	309.4
16	25.0	8.0	2.0	307	286	266	309.9
17	25.0	8.0	2.0	305	288	270	313.9
18	25.0	8.0	2.0	307	290	268	314.9
19	25.0	8.0	2.0	307	290	269	316.6
20	25.0	8.0	2.0	310	287	269	322.0

Figure 4.15. LOWTRAN7 results for observed total precipitable water versus calculated clear sky OLR with temperatures held constant for July 15, 1988 for selected sites over land. Linear regression using a least squares fit has been performed on the clear sky OLR data, and the correlation coefficient (r-value) is indicated.

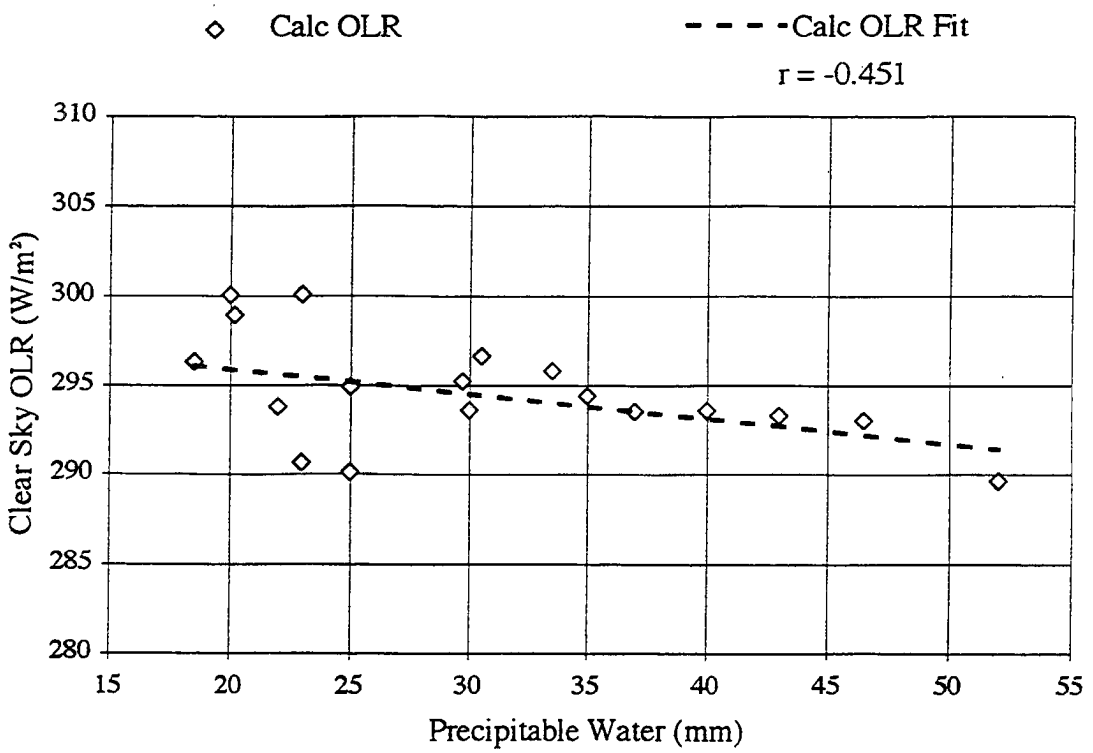

Table 4.4: Calculated values of clear sky OLR (W/m^2) for twenty LOWTRAN model runs. The calculated values were computed from observed values of precipitable water (mm) and constant temperatures (K) for a three-layer atmosphere of surface to 700 hPa, 700 to 500 hPa, and 500 to 300 hPa.

Test #	PW1 Sfc-700	PW2 700-500	PW3 500-300	Temp1 Sfc	Temp2 700 hPa	Temp3 500 hPa	OLR Calc
1	39.0	10.0	3.0	300	285	265	289.6
2	12.0	10.0	3.0	300	285	265	290.1
3	12.0	10.0	3.0	300	285	265	290.1
4	12.0	8.0	3.0	300	285	265	290.6
5	36.0	8.5	2.0	300	285	265	293.0
6	33.0	8.0	2.0	300	285	265	293.2
7	33.0	8.0	2.0	300	285	265	293.2
8	27.0	8.0	2.0	300	285	265	293.5
9	30.0	8.0	2.0	300	285	265	293.5
10	21.0	7.0	2.0	300	285	265	293.6
11	12.0	8.0	2.0	300	285	265	293.8
12	27.0	6.0	2.0	300	285	265	294.4
13	18.0	5.0	2.0	300	285	265	294.9
14	21.0	7.0	1.7	300	285	265	295.2
15	25.0	7.0	1.5	300	285	265	295.8
16	11.0	6.0	1.5	300	285	265	296.3
17	24.0	5.0	1.5	300	285	265	296.6
18	15.0	4.0	1.2	300	285	265	298.9
19	15.0	4.0	1.0	300	285	265	300.0
20	18.0	4.0	1.0	300	285	265	300.1

The middle and upper layers depicted in Figure 4.17 and Figure 4.18 more clearly reveal the negative correlation expected between water vapor and clear sky OLR. These levels are farther removed from the highly variable land surface and low-level horizontal advection of water vapor. Soden and Bretherton (1993) noted that the lower troposphere (below the 500 hPa level) is the primary source of water vapor for the upper troposphere, and that the vertical advection is responsible for transporting water vapor into the upper troposphere. Strong negative correlations of -0.933 in the 700 to 500 hPa layer, and -0.967 in the 500 to 300 hPa layer, exist between clear sky OLR and precipitable water. More water vapor at these levels leads to more infrared absorption and thus infrared emission at lower temperatures.

In all, the simulations confirmed both the positive and negative influences that temperature and precipitable water exert on clear sky OLR when examined separately. Surface and atmospheric temperatures exhibited a positive correlation with clear sky OLR under conditions of both varying and constant profiles of precipitable water. The strongest positive temperature correlations were found at the surface where temperatures are the warmest and under conditions where the precipitable water was held constant.

In the absence of temperature changes, an increase in precipitable water, especially at higher tropospheric levels, led to a decrease in top-of-the-atmosphere clear sky OLR. However, precipitable water is not an independent variable, but is itself a function of temperature as evidenced in the Clausius-Clapeyron equation. That is, an increase in temperature leads to an increase in the capacity of the air to retain water vapor. Thus, the highly variable nature of the land surface with regard to temperature clouded any direct relationship between precipitable water and clear sky OLR in the first simulation using observations.

This helps to explain why the water vapor/clear sky OLR signal is more strongly correlated over tropical and subtropical oceans than over land. The spatial and temporal stability found in sea surface temperatures and the overall homogeneity of the ocean surface

masks the dependence of precipitable water on the temperature. The decrease in clear sky OLR due to an increase in precipitable water in the absence of temperature variations reveals the effectiveness of water vapor as a greenhouse gas.

Figure 4.16. LOWTRAN7 results for observed surface to 700 hPa precipitable water versus calculated clear sky OLR with temperatures held constant for July 15, 1988 for selected sites over land. Linear regression using a least squares fit has been performed on the clear sky OLR data, and the correlation coefficient (r-value) is indicated.

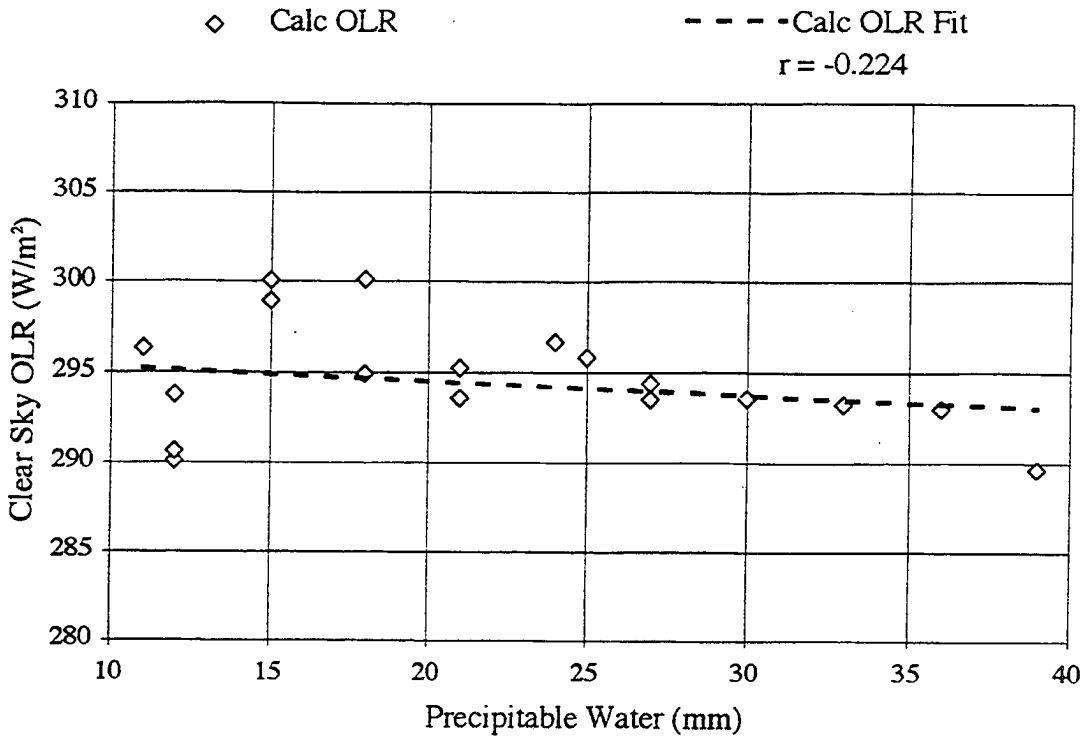

Figure 4.17. LOWTRAN7 results for observed 700 to 500 hPa precipitable water versus calculated clear sky OLR with temperatures held constant for July 15, 1988 for selected sites over land. Linear regression using a least squares fit has been performed on the clear sky OLR data, and the correlation coefficient (r-value) is indicated.

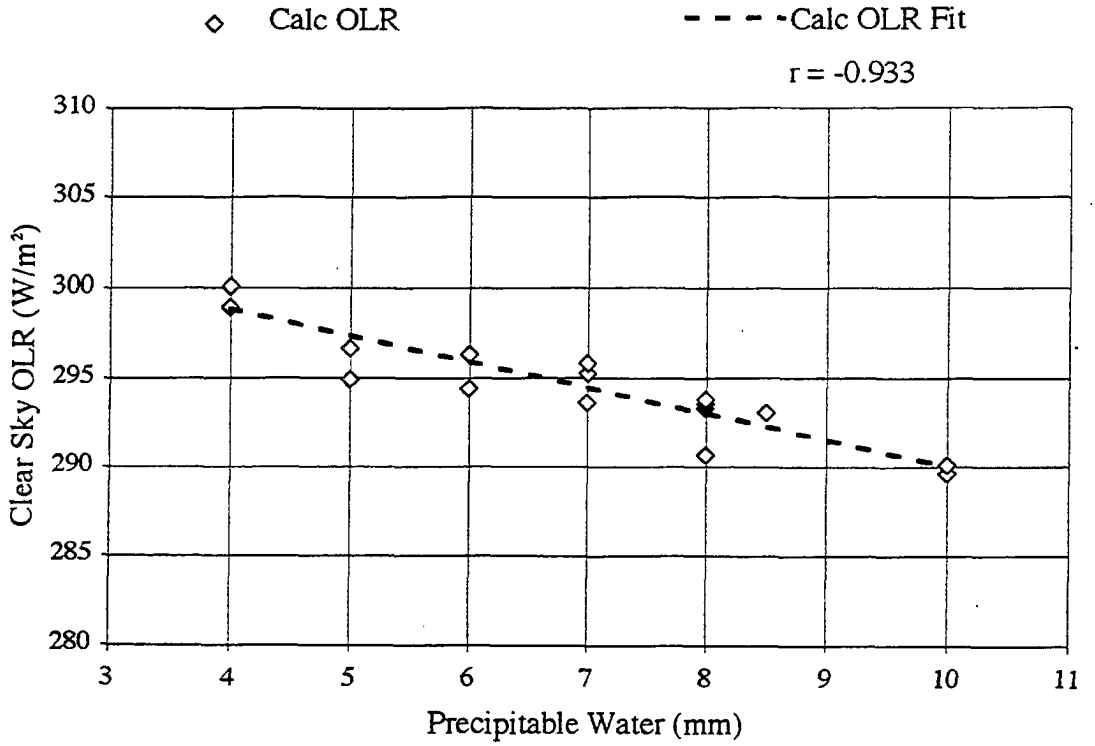

Figure 4.18. LOWTRAN7 results for observed 500 to 300 hPa precipitable water versus calculated clear sky OLR with temperatures held constant for July 15, 1988 for selected sites over land. Linear regression using a least squares fit has been performed on the clear sky OLR data, and the correlation coefficient (r-value) is indicated.

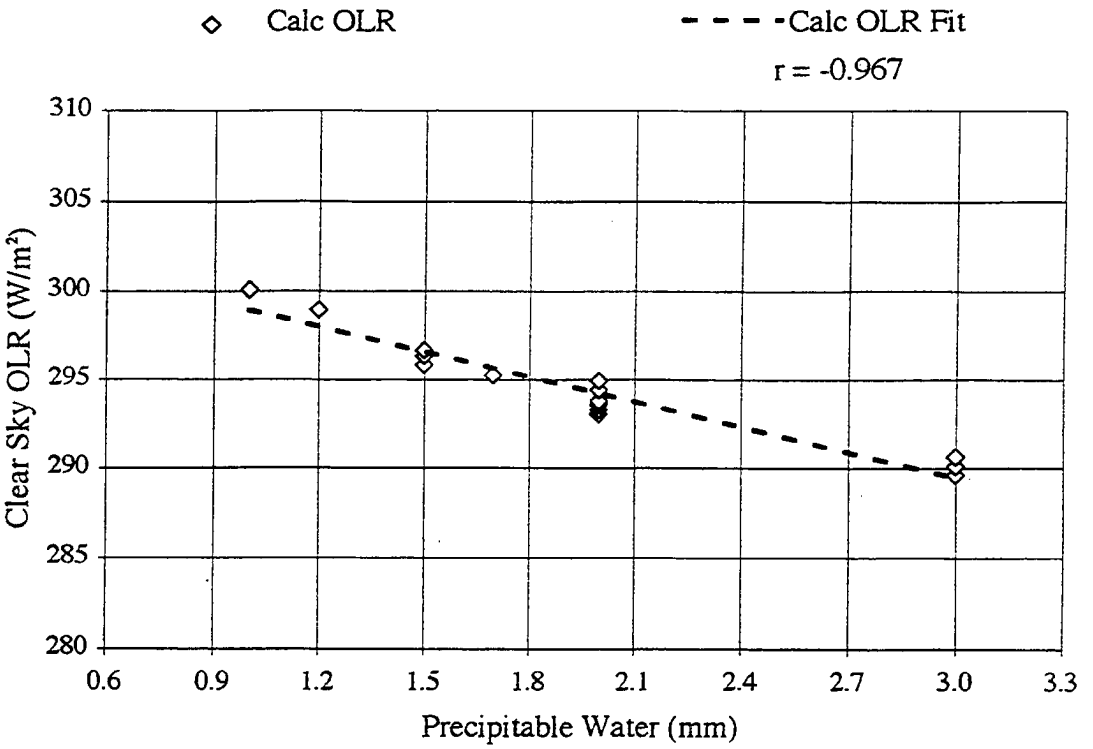

Chapter 5

CONCLUSION

This research examined the distribution, variability, and infrared radiative effects of atmospheric water vapor—the primary greenhouse gas. Water vapor is a highly variable quantity in time and space and has eluded accurate measurement on a global scale for quite some time. Radiosondes have reliably provided point measurements twice a day over land for the last 50 years, but a large void had existed over the oceans before the satellite era.

Satellites have greatly aided our characterization of global moisture fields. Coupled with radiosonde observations, satellite measurements of precipitable water have allowed us to fill in the missing pieces of the puzzle, and total global coverage on a daily basis has been achieved. Continued observations and processing of data will allow us to better describe precipitable water on a climatological time scale.

The merged precipitable water dataset used in this research provided an opportunity to examine the regional distribution and variability of atmospheric water vapor on a monthly basis. Regular patterns were found in the data corresponding to the latitudinal position, the nature of earth's surface below, the influence of the general circulation, and the effects of the seasons. These patterns generally matched the analyses done by a previous researcher using only radiosonde measurements. However, finer detail and greater surface influences were revealed in the present study which had the advantage of global satellite coverage. Ocean currents, movement of synoptic weather systems, elevated terrain, and seasonal cycles all exerted their influence on the pattern of precipitable water.

The availability of data also provided an opportunity to examine whether the signature of the great 1988 North American summer drought could be found in the monthly

means of precipitable water. Large and small differences in water vapor were found in the monthly averages between 1988 and 1989, but no large deficit of precipitable water was in evidence for the entire spring and summer of 1988. However, some indication was found that anomalous anticyclonic circulation caused the Midwest to be cut off from its primary moisture source—the Gulf of Mexico—during May and June of 1988. Precipitable water generally was available in 1988, but the atmospheric dynamics were lacking to produce rainfall from the vapor.

The second and third parts of this research focused on the radiative effect of water vapor, particularly its influence on clear sky outgoing longwave radiation. Water vapor's role as an atmospheric greenhouse gas causes it to reduce the amount of clear sky OLR escaping to space. Thus, our planet's surface is warmer than if there were no atmospheric water vapor. However, over mid-latitude land surfaces, the role of water vapor as a trapping greenhouse gas was not easily detectable due to the influence of temperature on the amount of atmospheric water vapor and magnitude of clear sky OLR. Use of the LOWTRAN7 radiative transfer model allowed the effects of temperature and water vapor on clear sky OLR to be examined separately. The ability of water vapor to trap infrared emission to space was clearly revealed when its dependence on temperature was removed.

OLR data were needed for the LOWTRAN7 simulations, yet accurate measurements of daily clear sky OLR over land were not produced by the ERBE averaging system due to insufficient sampling of the diurnal cycle. Data collected from ISCCP 10.7 μm temperature measurements were used to interpolate missing hourly ERBE values. Daily averages of clear sky OLR were used to calculate monthly means, and these showed general agreement with monthly averages that were produced by the ERBE averaging system.

The LOWTRAN7 radiative transfer model provided a means to investigate the relationships among surface and atmospheric temperatures, water vapor, and clear sky OLR over land using observations. Three simulations using 1) observed values of

temperature and precipitable water, 2) observed temperatures with constant values of precipitable water, and 3) observed values of precipitable water with constant temperature were run through the model. The desire in these radiation simulations was to use actual observations of temperature and water vapor to determine their effects on clear sky OLR.

Results from the first simulation indicated that temperature exerted the dominant influence on top-of-the-atmosphere clear sky OLR over land. Consistent with the Stefan-Boltzmann relationship, an increase in surface and atmospheric temperatures led to an increase in clear sky OLR. Further evaluation of the observations found that temperature was also responsible for the amount of precipitable water present. In general, the warmer temperatures were accompanied by higher values of precipitable water in the observations.

The second simulation in which the precipitable water content of the atmosphere was held fixed further verified the dominant influence of temperature on clear sky OLR. Results showed a strong positive correlation between temperature and clear sky OLR.

When temperatures were held constant in the third simulation, the radiative role of water vapor as a trapping greenhouse gas was revealed. In the absence of temperature variations, the expected relationship between water vapor and clear sky OLR over land became apparent. The negative correlation between water vapor and clear sky OLR strengthened with altitude reaching a maximum in the upper troposphere. In the middle, but especially in the upper reaches of the troposphere, an increase in water vapor was found to decrease the amount of clear sky OLR escaping to space. Total column precipitable water did not reveal as clear a negative correlation with OLR as did the individual layered amounts, especially in the upper troposphere.

What does the future hold? Continued data processing can provide us with a detailed water vapor climatology. Climatic means and anomalies will emerge more clearly as the database grows. The production of the three-layered precipitable water dataset opens the door for global moisture transport studies which were of limited scope previously. Finally, new satellite earth radiation budget instruments such as CERES will expand our

knowledge of the atmospheric radiation balance. New data will allow us to derive more accurate estimates of the clear sky greenhouse effect and water vapor's role in it. The ultimate goal of course, is to unlock the secrets of our climate. We will be better able to predict the natural and anthropogenic effects upon climatic feedbacks and be prepared for global climate changes.

REFERENCES

Bannon, J.K., B.A. and L.P. Steele, 1960: Average water-vapour content of the air. *Geophysical Memoirs No. 102*, British Meteorological Office, London.

Bohren, C.F., 1987: *Clouds in a Glass of Beer*. John Wiley & Sons, New York, 195 pp.

Bony, S. and J.P. Duvel, 1993: Influence of the vertical structure of the atmosphere on the seasonal variation of precipitable water and greenhouse effect. *Journal of Geophysical Research*, submitted.

Brooks, D.R. and P. Minnis, 1984: Comparison of longwave diurnal models applied to simulations of the Earth Radiation Budget Experiment. *Journal of Climate and Applied Meteorology*, **23**, 155-160.

Campbell, G.G., K. Dean, T. Greenwald, G. Stephens, and T.H. Vonder Haar, 1990: Science team report for the 27th ERBE meeting. Cooperative Institute for Research in the Atmosphere, Colorado State University.

Cess, R.D., 1989: Gauging water-vapour feedback. *Nature*, **342**, 736-737.

Cheruy, F., R.S. Kandel, and J.P. Duvel, 1991a: Outgoing longwave radiation and its diurnal variations from combined Earth Radiation Budget Experiment and Meteosat observations: 1. Estimating OLR from Meteosat data. *Journal of Geophysical Research*, **96**, 22,611-22,622.

Cheruy, F., R.S. Kandel, and J.P. Duvel, 1991b: Outgoing longwave radiation and its diurnal variations from combined Earth Radiation Budget Experiment and Meteosat observations: 2. Using Meteosat data to determine the longwave diurnal cycle. *Journal of Geophysical Research*, **96**, 22,623-22,630.

Coulson, K.L., 1975: *Solar and Terrestrial Radiation*. Academic Press, New York, 322 pp.

Elliott, W.P., D.J. Gaffen, J.D.W. Kahl, and J.K. Angell, 1994: The effect of moisture on layer thickness used to monitor global temperatures. *Journal of Climate*, **7**, 304-308.

Gaffen, D.J., T.P. Barnett, and W.P. Elliott, 1991: Space and time scales of global tropospheric moisture. *Journal of Climate*, **4**, 989-1008.

Galin, V.Y., V.M. Sutovskiy, and Y.M. Feygel'son, 1991: Relationships between outgoing and incoming integral IR radiation fluxes in clear skies. *Izvestiya, Atmospheric and Oceanic Physics*, **27**, 106-110.

Greenwald, T.J., G.L. Stephens, T.H. Vonder Haar, and D.L. Jackson, 1993: A physical retrieval of cloud liquid water over the global oceans using Special Sensor Microwave/Imager (SSM/I) observations. *Journal of Geophysical Research*, **98**, 18471-18488.

Kidder, S.Q. and T.H. Vonder Haar, 1992: *Satellite Meteorology: An Introduction.* To be published by Academic Press.

Kneizys, F.X., E.P. Shettle, L.W. Abreu, J.H. Chetwynd, G.P. Anderson, W.O. Gallery, J.E.A. Selby, and S.A. Clough, 1988: Users Guide to LOWTRAN7. Air Force Geophysics Laboratory, AFGL-TR-88-0177, Environmental Research Papers, No. 1010.

Manabe, S. and R.T. Wetherald, 1967: Thermal equilibrium of the atmosphere with a given distribution of relative humidity. *Journal of the Atmospheric Sciences*, **24**, 241-259.

Mielke, P.W., 1984: Meteorological applications of permutation techniques based on distance functions. *Handbook of Statistics, Vol. 4*, P.R. Krishnaiah and P.K. Sen, eds., North Holland, Amsterdam, 813-830.

Ottle, C. and M. Stoll, 1993: Effect of atmospheric absorption and surface emissivity on the determination of land surface temperature from infrared satellite data. *International Journal of Remote Sensing*, **14**, 2025-2037.

Peixoto, J.P. and A.H. Oort, 1992: *Physics of Climate.* American Institute of Physics, New York, 520 pp.

Peixoto, J.P. and A.H. Oort, 1983: The atmospheric branch of the hydrologic cycle and climate. *Variations in the Global Water Budget*, A. Street-Perrott *et al.*, eds., D. Reidel Publishing Company, Dordrecht, Holland, 5-65.

Peixoto, J.P., D.A. Salstein, and R.D. Rosen, 1981: Intra-annual variation in large-scale moisture fields. *Journal of Geophysical Research*, **86**, 1255-1264.

Peterson, T.C., 1991: The relationships between sea surface temperature anomalies and clouds, water vapor and their radiative effects. Colorado State University, Department of Atmospheric Science Paper No. 482.

Ramanathan, V., B.R. Barkstrom, and E.F. Harrison, 1989: Climate and the earth's radiation budget. *Physics Today*, 22-32.

Ramanathan, V. and W. Collins, 1991: Thermodynamic regulation of ocean warming by cirrus clouds deduced from observations of the 1987 El Niño. *Nature*, **351**, 27-32.

Randel, D.L., G.C. Campbell, and T.H. Vonder Haar, 1993: The effect of atmospheric water vapor on the observed outgoing longwave radiation: an observational study of water vapor forcing. Preprints, 4th Conference on Global Change Studies, AMS, Anaheim, California.

Randel, D.L., T.H. Vonder Haar, and G.L. Stephens, 1992: Combining multi-satellite measurements with different spatial and temporal resolutions into a new high-resolution water vapor data product. Conference Proceedings, International Symposium on Spectral Sensing Research, Maui, Hawaii, November 15-20, 1992.

Raval, A. and V. Ramanathan, 1989: Observational determination of the greenhouse effect. *Nature*, **342**, 758-761.

Reitan, C.H., 1960: Distribution of precipitable water vapor over the continental United States. *Bulletin American Meteorological Society*, **41**, 79-87.

Satran, J.E., D.R. Brooks, L. Maring, and S.K. Schaffner, 1986: Monthly time/space averaging. *Earth Radiation Budget Experiment Data Management System Reference Manual Volume VI—Daily Data Base and Monthly Time/Space Averaging*, NASA Langley Research Center.

Schiffer, R.A. and W.B. Rossow, 1983: The International Satellite Cloud Climatology Project (ISCCP): The first project of the World Climate Research Programme. *Bulletin of the American Meteorological Society*, **64**, 779-784.

Schluessel, P. and W.J. Emery, 1990: Atmospheric water vapour over oceans from SSM/I measurements. *International Journal of Remote Sensing*, **11**, 753-766.

Sellers, W.D., 1965: *Physical Climatology*. The University of Chicago Press, Chicago, 272 pp.

Soden, B.J. and F.P. Bretherton, 1993: Upper tropospheric relative humidity from the GOES 6.7 μm channel: Method and climatology for July 1987. *Journal of Geophysical Research*, **98**, 16,669-16,688.

Stephens, G.L., A. Slingo, and M.J. Webb, 1993: On measuring the greenhouse effect of earth. *High Spectral Resolution Infrared Remote Sensing for Earth's Weather and Climate Studies*, A. Chedin, M.T. Chahine, N.A. Scott, eds., Springer-Verlag, 395-417.

Trenberth, K.E., J.R. Christy, and J.G. Olson, 1987: Global atmospheric mass, surface pressure, and water vapor variations. *Journal of Geophysical Research*, **92**, 14,815-14,826.

Van de Griend, A.A. and M. Owe, 1993: On the relationship between thermal emissivity and the normalized difference vegetation index for natural surfaces. *International Journal of Remote Sensing*, **14**, 1119-1131.

Vonder Haar, T.H., D.L. Reinke, D.L. Randel, G.L. Stephens, C.L. Combs, M.I. Ringerud, I.L. Wittmeyer, and T.J. Greenwald, 1994: Total and layered global water vapor data set. AMS Seventh Conference on Satellite Meteorology and Oceanography, Monterey, California, June 6-10, 1994.

Webb, M.J., A. Slingo, and G.L. Stephens, 1993: Seasonal variations of the clear-sky greenhouse effect: the role of changes in atmospheric temperatures and humidities. Climate Research Technical Note No. 41.

Wittmeyer, I.L., 1990: Satellite based estimates of global precipitable water distribution and poleward latent heat flux. Colorado State University, Department of Atmospheric Science Paper No. 473.

Wittmeyer, I.L. and T.H. Vonder Haar, 1991: Analysis of the global ISCCP TOVS water vapor climatology. *Journal of Climate*, submitted.

Wu, M.L.C. and L.P. Chang, 1992: Longwave radiation budget parameters computed from ISCCP and HIRS2/MSU products. *Journal of Geophysical Research*, **97**, 10,083-10,101.